Effects of Atmospheric Turbulence on Spatially Entangled Photon Pairs Generated by SPDC

Jose Javier Fernández González

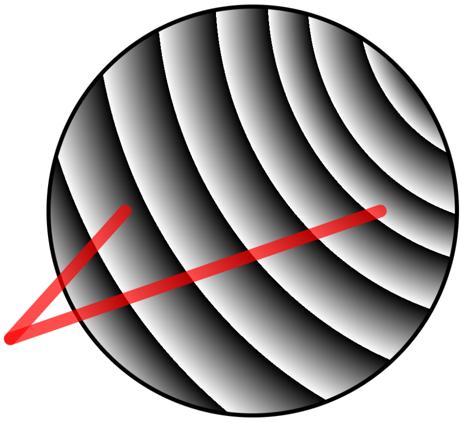

Master's Thesis
Supervisors
Jano Gil Lopez
Bruno Juliá Díaz

Space Communications —i2CAT

&

University of Barcelona

July 2026

Abstract

Spatially entangled photon pairs are promising resources for free-space quantum communication but, unlike polarization encoding, spatial encoding is directly affected by turbulence-induced wavefront distortions that reduce coherence between the spatial alternatives defining the quantum state. This thesis studies an effective two-qubit spatial state generated by degenerate Type-I spontaneous parametric down-conversion, in which signal and idler photons occupy two correlated transverse-path alternatives. Entanglement is quantified through concurrence, determined by the off-diagonal coherence of the two-photon density matrix. The atmosphere is modeled as an stochastic phase screen, and the change in concurrence is expressed as an ensemble average of phase differences evaluated at the four positions defining the spatial qubits. Theoretical predictions are derived from the phase structure functions of the Kolmogorov and modified von Kármán models, using the Fried parameter r_0 to characterize turbulence strength. Numerical phase screens are generated through a finite Zernike-polynomial expansion with correlated coefficients obtained from model-dependent covariance matrices. Simulations use 500 Zernike modes and 1,000 statistically independent phase screens for each sampled value of r_0. The numerical results agree closely with theory for both turbulence models. Concurrence approaches zero for strong turbulence and unity when the turbulent wavefront is coherent across the biphoton state. Entanglement degradation is governed mainly by the relation between r_0 and the effective transverse size $\Delta\rho'$, while the separation d between spatial alternatives has a weaker influence. Both turbulence models give similar predictions at the scales considered, with differences expected near the inner turbulence scale. The framework directly connects atmospheric phase statistics with spatial-entanglement degradation and provides a basis for more robust spatial encodings and future laboratory validation using spatial light modulators.

Keywords: spatial entanglement, spontaneous parametric down-conversion, atmospheric turbulence, concurrence, phase screens, Zernike polynomials, Fried parameter, Kolmogorov turbulence, modified von Kármán model, free-space quantum communication.

Acknowledgements

I would like to express my special thanks to my supervisor, Jano Gil, for his guidance, patience and continuous help throughout this work. His advice and support were essential in shaping the direction of this work and in helping me all along the way.

I would also like to thank Bruno Julia for his support during the project, and Xavier Jordán-Parra for giving me the opportunity to carry out this work. I am also grateful to Professor Robin Camphausen for his help, for the discussions we shared and for his valuable ideas, which contributed to the development of this thesis.

My deepest gratitude goes to my mother and father for their unconditional support, encouragement and for always pushing me to continue when things became difficult. And I would also like to thank my brothers, who inspire me to become a better version of myself and to show them what they can also achieve and much more. Thanks to my family in Barcelona, Jose and Odette, who recieved me just as my closest family from the very beginning.

And bittersweet a praise to all the friends who, from far away in Costa Rica and Guatemala, still believe in me, check on me, and give me the strength to continue pursuing my dreams even if that means setting an ocean between us. Thank you Alfredo, Alexa, Abraham, Felipe, Kaled, Melanie, Hoziecytw, Julián, and all the others who I carry in my heart.

I am also thankful to all the friends I have made along the way since the very beginning of this adventure and throughout all the stages that led me here. Their friendship and support made this last year one of the best periods of my life. My deepest gratitude goes to Ekaitz, Ender, Mar, Lidija, Blanca, Joaquín, Tino, Isadora, and all the other life-long friendships this stochastic world has let me build.

I would like to thank all the professors of the Master's programme for the knowledge they shared and for their contribution to my academic formation.

Finally, spatial thanks to the Flying Spaghetti Monster, whose noodly presence has undoubtedly guided this thesis to completion.

Contents

1 Introduction

Quantum technologies have become a relevant research field due to their potential impact on computation, communication, sensing and information security. In particular, quantum communication studies show that quantum states can be used to transmit information and correlations between distant parties, enabling protocols whose performance and security rely on the physical principles of quantum mechanics rather than only on computational complexity. This reliance offers security grounded in physical laws, like the measurement disturbance and the no-cloning theorem, that enables communication paradigms that are impossible to exploit through classical resources. One of the most representative examples is quantum key distribution (QKD), introduced with the BB84 protocol, which allows two users generate a secret key while detecting the presence of an eavesdropper through the disturbance produced by measurements on non-orthogonal quantum states [1, 2]. Even though QKD is one of the most mature applications of quantum communications, the field is broader and also includes entanglement distribution, high-dimensional encoding, quantum networks and other protocols based on the transmission of single photons or entangled photon pairs [3]. Recent advances in space quantum communication and satellite based QKD have brought up the interest in free space optical quantum links as a solution for long distance, and eventually global scale, quantum networks [4, 5]. These motivate the study of how quantum states of light propagate through realistic channels and, in particular, how atmospheric effects impact the properties that make them advantageous for quantum communications.

1.1 Quantum Communication Over Free Space Optical Channels

Once a quantum state has been generated and the information encoded, the performance of a quantum communications system is strongly determined by the physical channel through which the state is transmitted. Optical fiber is the most established transmission medium for terrestrial quantum links since it provides guided propagation, is compatible with existing telecommunication infrastructure and has relatively stable environmental conditions. However, fiber based quantum communication is limited by optical attenuation, which reduces the probability of detecting the transmitted photons as the propagation distance increases. Unlike classical optical communication, this loss can't be compensated without affecting the quantum state. For this reason, direct fiber links become increasingly inefficient over long distances, which motivates the use of alternative transmission channels for long range quantum networks [2, 4]

Free space optical (FSO) links provide one of the main alternatives to fiber transmission. In this case, the quantum states propagate through the atmosphere or through space rather than a guided medium, making FSO channels especially relevant for satellite-to-ground, ground-to-satellite, inter-satellite and terrestrial line-of-sight links. However, FSO presents its own challenges originating from diffraction, pointing errors, atmospheric absorption, scattering and turbulence, all of which modify the probability that a transmitted photon is collected and detected [4].

The initial motivation for this work is connected with the satellite QKD performance model proposed by Jordan-Parra et. al. [5], developed in the context of satellite-to-ground quantum communications. Their framework models the entire communication chain, including state preparation, free space propagation, receiver losses, and classical postprocessing, in order to estimate the final secret key generation performance metrics. In this type of model, the channel transmissivity is an important parameter, since it determines how many photons contribute to the detected signal. This makes the atmospheric effects a central part of quantum links performance analysis.

Although QKD has been discussed as a representative application, the present work is not centered on secret key generation but on the study of atmospheric turbulence as part of the free space optical channel, and on the development of phase masks that reproduce its effects under controlled experimental conditions. These phase masks can be used to simulate turbulence in laboratory studies of different quantum communication applications, including QKD, where atmospheric distortions affect beam propagation, collection efficiency and channel transmissivity [4, 6].

Various quantum communication applications exploit distinct encodings and protocols that are impacted differently by atmospheric turbulence. In systems such as polarization encoded QKD, turbulence is mainly considered as a source of loss. Meanwhile, other encoding schemes, with their own interesting applications, suffer from other turbulence induced effects on relative phase and spatial coherence, which directly degrades the quantum states carrying the information [7, 8]. Transverse spatial modes represent one such encoding, which has interesting applications in quantum communication protocols. However, the behavior of spatial correlations in turbulent environments remains understudied, making it a relevant study scenario for free space quantum communications.

1.2 Spatial Entanglement and Atmospheric Turbulence

Entanglement is one of the main resources used in quantum communications. In biphoton systems, entanglement may appear in different degrees of freedom, such as polarization, frequency, momentum or transverse position. Spatial entanglement is particularly interesting because it can provide access to higher dimension quantum states and spatial correlations that may be useful to transmit information encoded in higher dimension qudits instead of being limited to a two level qubit [7, 9, 10]. A common source of spatially entangled photon pairs is Spontaneous Parametric Down-Conversion (SPDC), where a pump photon in a non-linear crystal is converted into a pair of lower energy photons, usually called signal and idler. Due to the energy and momentum conservation, the generated photons present strong correlations in their transverse spatial variables [11, 12, 13].

These spatial correlations can be used to define effective two-qubit states based on alternative transverse paths, known as spatial modes (the physical setup generating these alternative paths is illustrated in Figure 1 and will be explained later in Section 2.3). In this description, the relevant information is not only the probability of detecting both photons in a given pair of paths, but also the coherence between the possible two-photon spatial modes. The degree of entanglement can be quantified through measures such as the concurrence, which depends on the off diagonal coherence terms of the two photon density matrix. This connects the optical coherence properties of the biphoton field with the quantum entanglement present in the spatial two qubit state [14, 15, 16].

When such a spatially entangled state propagates through the atmosphere, turbulence introduces random fluctuations of the refractive index. These fluctuations distort the optical wavefront and produce effects such as beam wander, scintillation and phase aberrations [6, 17]. For classical optical links, these effects are usually described in terms of intensity fluctuations, beam spreading or coupling losses. However, for spatially entangled quantum states the phase perturbations are relevant because of their affection in the spatial coherence in the two-photon system, thus degrading their entanglement [18].

A useful way to model this effect is to represent the atmosphere as a phase screen that multiplies the optical field by a random phase factor. In the case of spatially entangled two photon states, the turbulence contribution can be expressed through an ensemble average of phase differences evaluated at the transverse positions associated with the two alternatives, which modifies its concurrence. Therefore, the main problem addressed in this work is the simulation and characterization of this turbulence-induced reduction of spatial coherence [18].

To describe realistic atmospheric perturbations, statistical turbulence models are needed. The Kolmogorov model provides the classical description of refractive index fluctuations, while the von Kármán spectrum includes finite scale considerations that produces more accurate results. These spectra can be translated into phase statistics and summarized through parameters such as the Fried's parameter, which quantifies the effective strength of the turbulence along the propagation path and can be measured through meteorological stations [19, 6].

Since the phase perturbations are random, numerical phase screen generation is a practical tool for studying how different atmospheric conditions affect spatial quantum correlations, plus it can be implemented into an experimental setup through the use of a Spatial Light Modulator (SLM). This work follows a phase screen generation method based on Zernike polynomials, which provide a basis for describing optical aberrations over a circular aperture. It is possible to generate phase screens with controlled spatial statistics that follow either Kolmogorov or von Kármán models, and then be extended to dynamic turbulence [20, 17, 21].

The main objective of this work is therefore to build a consistent framework that connects spatially entangled photon pairs generated by SPDC, their description as spatially entangled two-qubit states, the degradation of their coherence by atmospheric turbulence, and the numerical generation of static and dynamic phase screens capable of reproducing the relevant atmospheric statistics. This provides a basis for studying the impact of turbulence on FSO links, and specifically spatially entangled states, beyond just an average loss description.

2 Theoretical Framework

2.1 Two-Qubit Entanglement

Quantum entanglement is a fundamental phenomenon where two or more parts of a system have non local correlations, meaning their quantum states cannot be described independently of one another, regardless of the spatial distance separating them. Two qubits may present different kinds of entanglement depending on the mode that is correlated between them, for example, a two qubit system with spin entanglement can be described as the superposition

$$|\psi\rangle = \alpha |\uparrow\rangle_1 |\downarrow\rangle_2 + \beta |\downarrow\rangle_1 |\uparrow\rangle_2 \tag{1}$$

where $|\uparrow\rangle_j$ and $|\downarrow\rangle_j$ represent the two spin states on qubit $j = 1, 2$, and the constants α, β are the respective probability amplitudes of the combined states. A measurement in this basis gives the outcome $|\uparrow\rangle_1 |\downarrow\rangle_2$ with probability $|\alpha|^2$, and the outcome $|\downarrow\rangle_1 |\uparrow\rangle_2$ with probability $|\beta|^2$. When both amplitudes are nonzero and the state cannot be factorized into a product of single qubit states, the two qubits are entangled.

Pure states, such as the one in Eq. (1), represent quantum systems whose state is completely specified by a single state vector $|\psi\rangle$. However, not every quantum state is pure. In many physical situations, the system must be described as a statistical mixture of possible pure states, where $|\psi_i\rangle$ occurs with probability p_i. This mixture is known as a *mixed state,* and its general representation is usually provided by the density matrix formalism:

$$\Omega = \sum_i p_i |\psi_i\rangle\langle\psi_i| , \tag{2}$$

with $p_i \geq 0$ and $\sum_i p_i = 1$.

Once a quantum state is represented by a density matrix, it is also necessary to distinguish between separable and entangled states. A two qubit state is separable if it can be written as a statistical mixture of product states of the two subsystems. If this is not possible, the state is entangled. Therefore, in addition to representing the state itself, an entanglement measurement is needed as a quantitative way to determine how much non classical correlation is present in the system.

One way to measure entanglement in a system is through the entanglement of formation. Conceptually, it quantifies the minimum number of maximally entangled Bell pairs needed to prepare a given state, which makes it a crucial metric in quantum communication for evaluating the usable quantum resources that survive transmission through a noisy channel. For mixed states, this quantity is the minimum average value of von Neumann entropy, which is defined as $E(\psi) = -\operatorname{tr}\{\psi_A \log_2 \psi_A\}$ with ψ_A as the partial trace of $|\psi\rangle\langle\psi|$ over either of the two subsystems, over all ensembles of Ω [15]. However, computing this minimum over all possible pure state decompositions is a complex problem that is difficult to handle analytically. Therefore, a more practical way of measuring entanglement that is related to the entanglement of formation is the Hill and Wootter's concurrence $\mathcal{C}$ [15, 16], which ranges from 0 to 1 and is monotonically related to E as $E(\Omega) = \mathcal{E}(\mathcal{C}(\Omega))$, where $\mathcal{E}$ is a monotone function obtained from the binary entropy function [16].

This way, the concurrence is an entanglement measure on its own, and can be defined for any mixed state Ω as [16]

$$\mathcal{C}(\Omega) = \max(0, \lambda_1 - \lambda_2 - \lambda_3 - \lambda_4) \tag{3}$$

where the λ_i values are the eigenvalues, sorted in decreasing order, of the Hermitian matrix $R = \sqrt{\sqrt{\Omega}\tilde{\Omega}\sqrt{\Omega}}$ (or alternatively the eigenvalues of the non-Hermitian matrix $\Omega\tilde{\Omega}$). In this context, $\tilde{\Omega} = (\sigma_y \otimes \sigma_y)\Omega^*(\sigma_y \otimes \sigma_y)$ represents the spin-flipped density matrix, with σ_y being the Pauli matrix Y:

$$\sigma_y = \begin{pmatrix} 0 & -i \\ i & 0 \end{pmatrix} . \tag{4}$$

2.2 Spontaneous Parametric Down-Conversion

Spontaneous parametric down-conversion (SPDC) is a phenomenon that occurs in non-linear crystals in which a single photon undergoes a frequency conversion process with a certain probability to "split" into a pair of photons with lower energy [11]. The conventional naming for these photons are *pump (p)* for the higher energy photon, and *signal (s)* and *idler (i)* for the lower energy resulting photons. For SPDC to occur, the process has to fulfill the phase-matching condition: $\boldsymbol{k}_p = \boldsymbol{k}_s + \boldsymbol{k}_i$; and energy conservation: $\omega_p = \omega_s + \omega_i$. For the degenerate case, which is being considered in this work, $\omega_s = \omega_i = \omega_p/2$.

From a quantum formalism, the state of the crystal before SPDC can be seen as

$$|\psi_0\rangle = |\alpha\rangle_p |0\rangle_s |0\rangle_i , \tag{5}$$

where $|\alpha\rangle_p$ describes a coherent state in the pump, meaning it doesn't get affected by the destruction of its single photons. This can be assumed because the SPDC process is very inefficient since it has a low probability of happening, thus the amount of photons taken out from the pump is negligible. The states $|0\rangle_s$ and $|0\rangle_i$ describe the vacuum state for signal and idler photons.

The quantum Hamiltonian of the electromagnetic field in the SPDC crystal can be described as [13]

$$\hat{H} = \sum_{\mathbf{k},\gamma} \hbar\omega(\mathbf{k}) \hat{a}^{\dagger}_{\mathbf{k},\gamma} \hat{a}_{\mathbf{k},\gamma} + \frac{\epsilon_o}{2} \int \mathrm{d}^3 r \; \tilde{\chi}^{(2)}_{psi} \hat{E}_p(\mathbf{r_p}, t) \hat{E}_s(\mathbf{r_s}, t) \hat{E}_i(\mathbf{r_i}, t), \tag{6}$$

where the first term is the linear contribution of each photon $\gamma \in \{p, s, i\}$ and the second term corresponds to the non-linear part with $\tilde{\chi}^{(2)}_{psi}$ as the non-linear susceptibility that depends on the frequency of the pump, signal and idler, and the electric field observables $\hat{E}$ for each. These observables can be separates into its positive and negative frequency contributions as $\hat{E} = \hat{E}^{(+)} + \hat{E}^{(-)}$ so that $\hat{E}^{(+)}$ contains an annihilation operator $\hat{a}_{\mathbf{k},\gamma}$ and $\hat{E}^{(-)} = [\hat{E}^{(+)}]^*$ contains a creation operator $\hat{a}^{\dagger}_{\mathbf{k},\gamma}$. [22]

Since the pump is a coherent state, which is an eigenstate of both $\hat{E}^{(+)}$ and $\hat{E}^{(-)}$, the electric field associated with the signal and idler are the negative frequency ones, thus, the SPDC is described quantum mechanically as an annihilation of the pump photon and creation of a signal-idler pair, so that the resulting biphoton state for a thin crystal can be described as [11, 12, 23]

$$|\psi_{SPDC}\rangle = C_1 |0\rangle_s |0\rangle_i + C_2 \iint d\boldsymbol{q_s} d\boldsymbol{q_i} \nu(\boldsymbol{q_s} + \boldsymbol{q_i}) |\boldsymbol{q_s}, \sigma_s\rangle_s |\boldsymbol{q_i}, \sigma_i\rangle_i \tag{7}$$

where C_1, C_2 are constants, $\boldsymbol{q_s}, \boldsymbol{q_i}$ are the transverse components of momentum (k_x, k_y), and σ_s, σ_i are the polarizations of signal and idler photons respectively. The angular spectrum of the pump laser $\nu(\boldsymbol{q_s} + \boldsymbol{q_i})$ is then transferred to the created single photons, and so they inherit its spatial properties [12]. The resulting photons are spatially entangled in their momenta, as can be identified in the second term of the system [11, 12, 23, 24].

There exist different types of SPDC depending on the polarization of the signal and idler photons with respect to the pump polarization [25]. This type classification also indicates the spatial distribution of the resulting photons. For our case-study we will consider a Type-I SPDC process as is often the case in quantum information experiments [13], meaning the signal and idler photons are generated at opposite directions along the pump laser axis following the respective phase-matching conditions.

2.3 Spatial Two-Qubit States

The previous sections introduced two elements needed for the model used in this work. First, the concurrence provides a quantitative measure of entanglement for two qubit states. Second, SPDC generates photon pairs with strong correlations in their transverse spatial variables. However, the transverse position and momentum degrees of freedom are continuous, while the concurrence formalism introduced above applies to a finite two qubit system. To connect these descriptions, one can define an effective spatial qubit for each photon by selecting two alternative transverse paths, or spatial modes $(\boldsymbol{\rho}_{s1}, \boldsymbol{\rho}_{s2}, \boldsymbol{\rho}_{i1}, \boldsymbol{\rho}_{i2})$. The biphoton state is then described using a discrete basis associated with the possible signal and idler path combinations, while the coherence between these alternatives determines the amount of spatial entanglement [14].

In this work, we consider the setup proposed by Jha and Boyd [14] as shown in the Figure 1. An SPDC crystal is illuminated with a pump laser, generating pairs of signal and idler photons with transverse spatial correlations. Each photon may propagate through one of two alternative paths (labelled 1 and 2) before reaching its corresponding detectors.

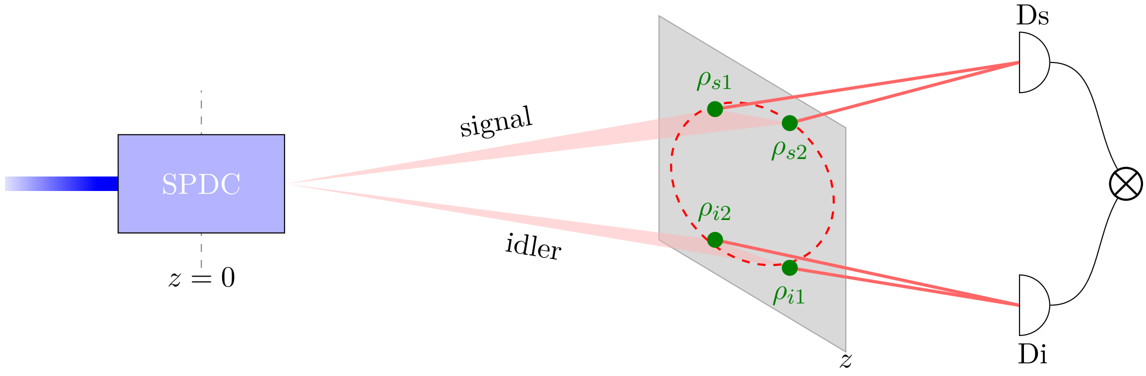

Figure 1: Diagram of two spatially entangled qubits preparation via SPDC. The aperture positions are selected so that the correlated alternative transverse paths $(\boldsymbol{\rho}_{s1}, \boldsymbol{\rho}_{i1})$ and $(\boldsymbol{\rho}_{s2}, \boldsymbol{\rho}_{i2})$ dominate, while the cross alternatives transverse paths $(\boldsymbol{\rho}_{s1}, \boldsymbol{\rho}_{i2})$ and $(\boldsymbol{\rho}_{s2}, \boldsymbol{\rho}_{i1})$ are negligible.

The four possible combinations of signal and idler paths define the spatial basis $\{|\boldsymbol{\rho}_{s1}, \boldsymbol{\rho}_{i1}\rangle\,; |\boldsymbol{\rho}_{s1}, \boldsymbol{\rho}_{i2}\rangle\,; |\boldsymbol{\rho}_{s2}, \boldsymbol{\rho}_{i1}\rangle\,; |\boldsymbol{\rho}_{s2}, \boldsymbol{\rho}_{i2}\rangle\}$. However, the SPDC source and the transverse position of the apertures are chosen so that the generated photons are strongly correlated in position. As a result, the probability amplitudes associated with the cross alternatives $|\boldsymbol{\rho}_{s1}, \boldsymbol{\rho}_{i2}\rangle$ and $|\boldsymbol{\rho}_{s2}, \boldsymbol{\rho}_{i1}\rangle$ are negligible compated with the correlated alternatives $|\boldsymbol{\rho}_{s1}, \boldsymbol{\rho}_{i1}\rangle$ and $|\boldsymbol{\rho}_{s2}, \boldsymbol{\rho}_{i2}\rangle\}$. Therefore, the density matrix is written as

$$\Omega_{\text{tp}} = \begin{pmatrix} a & 0 & 0 & c \\ 0 & 0 & 0 & 0 \\ 0 & 0 & 0 & 0 \\ d & 0 & 0 & b \end{pmatrix}, \tag{8}$$

where a is the probability that the signal and idler photons are detected in $|\boldsymbol{\rho}_{s1}, \boldsymbol{\rho}_{i1}\rangle$, b is the probability that the signal and idler photons are detected in $|\boldsymbol{\rho}_{s2}, \boldsymbol{\rho}_{i2}\rangle$, and c is a measure of coherence between the states $|\boldsymbol{\rho}_{s1}, \boldsymbol{\rho}_{i1}\rangle$ and $|\boldsymbol{\rho}_{s2}, \boldsymbol{\rho}_{i2}\rangle$. Consider that since density matrices are hermitic and $\text{tr}\{\Omega_{tp}\} = 1$, then $a + b = 1$, where a, b are both real quantities and $c = d^*$.

The electric fields present at the detectors for signal and idler photons $\gamma \in \{s, i\}$ can be described as [14]

$$\hat{E}_\gamma^{(+)}(\boldsymbol{r}_\gamma, t) = k_{\gamma 1}\hat{E}_{\gamma 1}^{(+)}(\boldsymbol{r}_{\gamma 1})e^{-i\omega_\gamma(t-t_{\gamma 1})} + k_{\gamma 2}\hat{E}_{\gamma 2}^{(+)}(\boldsymbol{r}_{\gamma 2})e^{-i\omega_\gamma(t-t_{\gamma 2})}, \tag{9}$$

where $k_{\gamma 1}, k_{\gamma 2}$ are constants that depend on the physical size and geometry of the holes at transversal positions $\boldsymbol{\rho}_{\gamma 1}, \boldsymbol{\rho}_{\gamma 2}$; and the positive frequency electric fields associated with annihilation operators are considered since photons are being absorbed by the detectors. Note that $\boldsymbol{r}_\gamma = (\boldsymbol{\rho}_\gamma, z)$.

The probability per unit of time squared that a signal photon is detected at $\boldsymbol{r}_s$ at a time t and an idler photon at $\boldsymbol{r}_i$ at a time t' is known as the coincidence count rate [22]:

$$R_{si}(\boldsymbol{r}_s, \boldsymbol{r}_i) = \alpha_s\alpha_i\,\text{tr}\{\Omega_{\text{tp}}\hat{E}_s^{(-)}(\boldsymbol{r}_s, t)\hat{E}_i^{(-)}(\boldsymbol{r}_i, t')\hat{E}_i^{(+)}(\boldsymbol{r}_i, t')\hat{E}_s^{(+)}(\boldsymbol{r}_s, t)\}, \tag{10}$$

where α_s, α_i are the quantum efficiencies of the detectors. Thus, using the expression from Eq. (9) one can derive the expression for the count rate [14]:

$$R_{si}(\boldsymbol{r}_s, \boldsymbol{r}_i) = k_1^2 S^{(2)}(\boldsymbol{r}_{s1}, \boldsymbol{r}_{i1}) + k_2^2 S^{(2)}(\boldsymbol{r}_{s2}, \boldsymbol{r}_{i2}) + k_1 k_2 W^{(2)}(\boldsymbol{r}_{s1}, \boldsymbol{r}_{i1}, \boldsymbol{r}_{s2}, \boldsymbol{r}_{i2}) \times e^{i[\omega_s(t_{s1}-t_{s2})+\omega_i(t_{i1}-t_{i2})]} + \text{c.c.}, \tag{11}$$

where c.c. indicates the complex conjugate of the last term, constants are grouped as $k_1 = \sqrt{\alpha_s \alpha_i} k_{s1} k_{i1}$ and $k_2 = \sqrt{\alpha_s \alpha_i} k_{s2} k_{i2}$,

$$W^{(2)}(\boldsymbol{r}_{s1}, \boldsymbol{r}_{i1}, \boldsymbol{r}_{s2}, \boldsymbol{r}_{i2}) = \text{tr}\{\Omega_{\text{tp}} \hat{E}_{s1}^{(-)}(\boldsymbol{r}_{s1}) \hat{E}_{i1}^{(-)}(\boldsymbol{r}_{i1}) \hat{E}_{i2}^{(+)}(\boldsymbol{r}_{i2}) \hat{E}_{s2}^{(+)}(\boldsymbol{r}_{s2})\} \tag{12}$$

is known as the the two-photon cross-spectral density function and

$$S^{(2)}(\boldsymbol{r}_{s1}, \boldsymbol{r}_{i1}) = W^{(2)}(\boldsymbol{r}_{s1}, \boldsymbol{r}_{i1}, \boldsymbol{r}_{s1}, \boldsymbol{r}_{i1}) \tag{13}$$

as the two-photon spectral density.

The two-photon cross-spectral density function $W^{(2)}$ is a very important expression, since it allows for quantifying the coherence between the two photons. One can actually map the term from Eq. (11) to their physical meaning in the two qubit density matrix expression [14]: taking a proportionality constant accounting for the total rate as

$$\eta = \left[k_1^2 S^{(2)}(\boldsymbol{r}_{s1}, \boldsymbol{r}_{i1}) + k_2^2 S^{(2)}(\boldsymbol{r}_{s2}, \boldsymbol{r}_{i2})\right]^{-1} \tag{14}$$

it becomes evident that the probability of the two photon state being in the different alternative paths and the coherence between both alternatives when arriving at the same time at the detector are

$$a = \eta k_1^2 S^{(2)}(\boldsymbol{r}_{s1}, \boldsymbol{r}_{i1}) \tag{15}$$
$$b = \eta k_2^2 S^{(2)}(\boldsymbol{r}_{s2}, \boldsymbol{r}_{i2}) \tag{16}$$
$$c = \eta k_1 k_2 W^{(2)}(\boldsymbol{r}_{s1}, \boldsymbol{r}_{i1}, \boldsymbol{r}_{s2}, \boldsymbol{r}_{i2}). \tag{17}$$

Now, considering the concurrence $\mathcal{C}$ as our entanglement measurement [14], we may apply the spin-flip transformation to the two-qubit density matrix:

$$\tilde{\Omega}_{\text{tp}} = (\sigma_y \otimes \sigma_y) \Omega_{\text{tp}}^* (\sigma_y \otimes \sigma_y) \tag{18}$$
$$= \begin{pmatrix} b^* & 0 & 0 & d^* \\ 0 & 0 & 0 & 0 \\ 0 & 0 & 0 & 0 \\ c^* & 0 & 0 & a^* \end{pmatrix}. \tag{19}$$

And taking the simplified matrix (taking $c = d^*$ and real values for a, b)

$$\Omega_{\text{tp}} \tilde{\Omega}_{\text{tp}} = \begin{pmatrix} ab + |c|^2 & 0 & 0 & 2ac \\ 0 & 0 & 0 & 0 \\ 0 & 0 & 0 & 0 \\ 2bc^* & 0 & 0 & ab + |c|^2 \end{pmatrix}, \tag{20}$$

with eigenvalues

$$\lambda_1 = (\sqrt{ab} + |c|)^2, \tag{21}$$

$$\lambda_2 = (\sqrt{ab} - |c|)^2, \tag{22}$$

$$\lambda_{3,4} = 0. \tag{23}$$

Then, using Eq. (3) we find the expression for concurrence for our two qubit system as

$$\mathcal{C}(\Omega_{\text{tp}}) = 2|c|. \tag{24}$$

And in terms of spectral densities given our setup:

$$\mathcal{C}(\Omega_{\text{tp}}) = \frac{2k_1k_2|W^{(2)}(\boldsymbol{r}_{s1}, \boldsymbol{r}_{i1}, \boldsymbol{r}_{s2}, \boldsymbol{r}_{i2})|}{k_1^2 S^{(2)}(\boldsymbol{r}_{s1}, \boldsymbol{r}_{i1}) + k_2^2 S^{(2)}(\boldsymbol{r}_{s2}, \boldsymbol{r}_{i2})}. \tag{25}$$

2.4 Effect of Atmospheric Turbulence on Spatial Entanglement

For the setup described in the Figure 1, we will consider that the two photons travel through a turbulent atmosphere before reaching the detectors. The effect of the turbulence can be accounted for by considering a phase change in propagating light at plane z such that it modifies the electric field's expression [26]:

$$\hat{\tilde{E}}^{(+)}(\boldsymbol{r}) = e^{i\phi(\boldsymbol{r})}\hat{E}^{(+)}(\boldsymbol{r}), \tag{26}$$

where $\phi(\boldsymbol{r})$ is the phase value introduced by the atmosphere at each transversal position. Now, with this consideration we can obtain an expression for Eq. (12) that takes phase changes into account as:

$$\begin{aligned} W^{(2)}(\boldsymbol{r}_{s1}, \boldsymbol{r}_{i1}, \boldsymbol{r}_{s2}, \boldsymbol{r}_{i2}) = &\left\langle e^{-i[\phi(\boldsymbol{r}_{s1}) - \phi(\boldsymbol{r}_{s2}) + \phi(\boldsymbol{r}_{i1}) - \phi(\boldsymbol{r}_{i2})]}\right\rangle \\ &\times \text{tr}\{\Omega_{\text{tp}}\hat{E}_{s1}^{(-)}(\boldsymbol{r}_{s1})\hat{E}_{i1}^{(-)}(\boldsymbol{r}_{i1})\hat{E}_{i2}^{(+)}(\boldsymbol{r}_{i2})\hat{E}_{s2}^{(+)}(\boldsymbol{r}_{s2})\}. \end{aligned} \tag{27}$$

As we can see, the effect of the turbulence from the atmosphere can be accounted for by a single parameter we may denote as [18]:

$$\mu_{\text{turb}} = \left\langle e^{-i[\phi(\boldsymbol{r}_{s1}) - \phi(\boldsymbol{r}_{s2}) + \phi(\boldsymbol{r}_{i1}) - \phi(\boldsymbol{r}_{i2})]}\right\rangle. \tag{28}$$

The turbulence factor introduced above shows how atmospheric phase fluctuations eaffect the coherence term of spatial two qubit state. To evaluate this quantity, the random phase must be related to realistic atmospheric turbulence statistics. This requires a model for refractive index fluctuations in the atmosphere and for the corresponding phase distortions accumulated during propagation.

2.5 Atmospheric Turbulence Models

Atmospheric turbulence emerges from random fluctuations of temperature and pressure, which produce local variations of the refractive index [27]. As light propagates through the turbulent medium, different parts of the wavefront accumulate different phases. In this work, these phase fluctuations are the relevant atmospheric effect, since they modify the relative phases between spatial alternatives of the biphoton state.

To describe these fluctuations statistically, the power spectral density $\Phi_n(k)$ of the refractive-index fluctuations is used [6]. This function indicates how the turbulence strength is distributed among different spatial scales. The scalar wavenumber k is related to a characteristic turbulent eddy current of size L through $k = \frac{2\pi}{L}$, so that small values of k correspond to large scale refractive index variations, and large values of k correspond to small scale variations. In isotropic turbulence, the spectrum depends only on the magnitude k, not on its direction [6]. Kolmogorov theory describes the inertial subrange of atmospheric turbulence, where energy is transferred from large eddies to smaller ones without significant energy injection or viscous dissipation. In this range, the refractive index spectrum follows

$$\Phi_n(k) \propto C_n^2 k^{-11/3}. \tag{29}$$

where C_n^2 is the refractive index structure constant, which represents the strength of the atmospheric fluctuations. This expression is valid between the outer and inner turbulence scales. For $k < k_0$, eddies larger than the outer scale $L_0 = \frac{2\pi}{k_0}$, the Kolmogorov theory does not predict the spectral shape. For $k > k_m$, corresponding to eddies smaller than the inner scale $l_0 = \frac{2\pi}{k_m}$, viscosity becomes relevant and the spectrum decays rapidly. [6]

Assuming $L_0 \to \infty$ and $l_0 \to 0$ gives the Kolmogorov limit, while the more realistic modified von Kármán spectrum is defined as

$$\Phi_n(k, z) = 0.00969\, C_n^2(z)\, \frac{\exp\left[-\left(\frac{2\pi k l_0}{5.92}\right)^2\right]}{\left(k^2 + L_0^{-2}\right)^{11/6}}. \tag{30}$$

For a thin turbulent layer and a plane wave, this refractive-index spectrum is converted into a phase spectrum by the optical wavenumber factor $(2\pi/\lambda)^2$. After integrating the turbulence strength into Fried's parameter r_0, the phase spectrum can be written as [21]

$$\Phi(k) = 0.0229\, r_0^{-5/3}\, \frac{\exp\left[-\left(\frac{2\pi k l_0}{5.92}\right)^2\right]}{\left(k^2 + L_0^{-2}\right)^{11/6}}. \tag{31}$$

This expression connects the atmospheric turbulence model and the random phase $\phi(\boldsymbol{r})$ introduced in the previous section. The spectrum $\Phi(k)$ determines how strongly each spatial frequency contributes to the phase screen, while the parameter r_0 sets the overall strength of the phase fluctuations. Therefore, smaller values of r_0 correspond to stronger wavefront distortions and to larger phase differences between separated transverse positions of the two photon state.

The Fried parameter is a compact way of expressing the integrated turbulence strength along the propagation path. Physically, it represents the characteristic transverse length over which the propagating light keeps approximately coherent phase [28]. For a path of length L it is

$$r_0 = \left[0.423 \left(\frac{2\pi}{\lambda}\right)^2 \int_0^L C_n^2(z) \left(1 - \frac{z}{L}\right)^{\frac{5}{3}\delta_{\rm sp}} dz\right]^{-3/5}, \tag{32}$$

where $\delta_{\rm sp} = 0$ for a plane wave and $\delta_{\rm sp} = 1$ for a spherical wave. In the homogeneous plane-wave case, C_n^2 is constant along the path and $\delta_{\rm tp} = 0$ so the integral reduces to the dependence on $C_n^2 L$. Therefore, the turbulence induced phase distortions increase with both the refractive index fluctuation strength and the propagation distance.

3 Phase Screens Generation Methodology

The previous section established how atmospheric turbulence affects spatially entangled two photon states via phase fluctuations introduced by the atmosphere or turbulent media. It also introduced the turbulence models used to describe those fluctuations statistically with Fried's parameter r_0 as a compact measure of turbulence strength. However, in order to evaluate this effect numerically and apply it to the spatial two qubit system, these statistical models have to be converted into explicit realizations of the turbulent phase $\phi(\boldsymbol{\rho})$. This section describes the methodology for this conversion. Phase screens are used as numerical representations of the atmospheric phase perturbations over a transverse plane.

There are different methods for creating the phase screens that simulate turbulent atmospheric effects. Two of the most commonly used methods are the Fourier Series and the Zernike polynomials as basis sets. The main drawback of the Fourier Series method is that it doesn't adequately account for low frequencies that shift the centroid of a propagating beam, known as beam wander [29]. Although there are ways for solving this and other issues with this method, such as the addition of subharmonics and random midpoint displacement, the Zernike polynomials provide in general a more accurate simulation of Kolmogorov turbulence [29].

This work follows the Zernike-based methodology of Lu and Cai [21], where the phase screen is generated from Zernike coefficients correlated through a covariance matrix derived from the modified von Kármán spectrum, and the time evolution is drawn from temporal power spectra.

The developed framework includes also the generation of dynamic phase screens through time dependent Zernike coefficients and atmospheric wind parameters. However, this extension is not required for the concurrence calculations presented in this work. Since concurrence is obtained from an ensemble average of phase realizations with fixed atmospheric statistics, the temporal order of the generated screens does not modify the final averaged result. For this reason, the dynamic phase generation method is presented in Appendix A. This extension may still be useful for future studies involving time dependent propagation effects or experimental implementations where the temporal evolution of turbulence needs to be reproduced.

3.1 Zernike Basis

Zernike polynomials can be used to describe optical aberrations, such as piston (constant phase shift), tilt, defocus, etc. [17] as shown in Table 1.

Table 1: Optical aberrations classified by Noll index, radial degree, and azimuthal frequency

Noll index j	Radial degree n	Azimuthal frequency m	Optical Aberration
1	0	0	Piston
2, 3	1	1	Tilt
4	2	0	Defocus
5, 6	2	2	Astigmatism
7, 8	3	1	Pure Coma
9, 10	3	3	Zero Curvature Coma
11	4	0	Spherical
12, 13	4	2	5^{th} order Astigmatism

The single index j is only a compact ordering of the two Zernike indices (n, m). The radial degree n determines the order of the radial polynomial, while the azimuthal frequency m determines the angular dependence. Only pairs satisfying $0 \le m \le n$ and $n-m$ even are allowed. For $m = 0$ there is one radial mode, while for $m > 0$ there are two real modes with the same (n, m), one proportional to $\cos(m\theta)$ and the other to $\sin(m\theta)$. Following Noll's convention, the modes are ordered by increasing radial degree n, so that $j = 1$ corresponds to piston, $j = 2, 3$ to the two tilt modes, $j = 4$ to defocus, and so on. Therefore, the phase over a circular aperture is expanded in real Zernike modes as [20]

$$\phi(\boldsymbol{\rho}) = \sum_{j=2}^{N} a_j Z_j(\rho, \theta), \tag{33}$$

where $\boldsymbol{\rho}$ is a coordinate in the pupil at radius ρ and angle θ, a_j is the Zernike coefficient, and N is the highest mode kept in the simulation. The piston term is ignored because a constant phase offset does not change the turbulence effects that matter in this study, so the expansion starts at $j = 2$.

Using Noll indexing, the real Zernike functions are written as [20, 21]

$$Z_j(\rho, \theta) = \begin{cases} \sqrt{2(n+1)}\, R_n^m(\rho) \cos(m\theta), & m \neq 0,\ j \text{ even}, \\ \sqrt{2(n+1)}\, R_n^m(\rho) \sin(m\theta), & m \neq 0,\ j \text{ odd}, \\ \sqrt{n+1}\, R_n^0(\rho), & m = 0. \end{cases} \tag{34}$$

The direct expression for the radial polynomial is

$$R_n^m(\rho) = \sum_{s=0}^{(n-m)/2} \frac{(-1)^s (n-s)!}{s!\,\left(\frac{n+m}{2} - s\right)!\,\left(\frac{n-m}{2} - s\right)!} \rho^{n-2s}. \tag{35}$$

This expression becomes slow and numerically fragile for higher order modes as it sums larger terms. To avoid this, the recursive approach discussed by Lu and Cai and later tested in more detail by Li et al. uses the recurrence [21, 30]

$$R_n^m(\rho) = \rho \left[R_{n-1}^{|m-1|}(\rho) + R_{n-1}^{m+1}(\rho) \right] - R_{n-2}^m(\rho), \tag{36}$$

with $R_0^0(\rho) = 1$ and invalid terms set to zero. This keeps the calculation stable when the number of modes is increased.

3.2 Stationary Coefficient Statistics

In the Zernike-based method, the coefficients are generally not statistically independent. The covariance between modes has to be included, especially when the screen is generated from a finite number of modes [17, 21].

For the modified von Kármán spectrum, Lu and Cai provide the covariance between two Zernike coefficients as

$$\begin{aligned} C_{jj'} = \left\langle a_j a_{j'}^* \right\rangle = (-1)^{(n+n'-2m)/2} \delta_z \frac{0.0458}{\pi} \left(\frac{R}{r_0} \right)^{5/3} \sqrt{(n+1)(n'+1)} \\ \times \int_0^\infty df \frac{J_{n+1}(2\pi f) J_{n'+1}(2\pi f)}{f \left[f^2 + (R/L_0)^2 \right]^{11/6}} \exp\left[-\left(\frac{2\pi f l_0}{5.92R} \right)^2 \right]. \end{aligned} \tag{37}$$

Here J_n is a Bessel function of the first kind, r_0 is the Fried parameter, L_0 is the outer scale, and l_0 is the inner scale. The selector δ_z is one only when the two modes are allowed to be correlated:

$$\delta_z = (m = m') \cap \left[\text{parity}(j, j') \cup (m = 0)\right]. \tag{38}$$

If $L_0 \to \infty$ and $l_0 \to 0$, Eq. (37) reduces to the Kolmogorov/Roddier result [17]. This is useful as a limiting case and as a quick consistency check.

Once all $C_{jj'}$ are computed, they form the covariance matrix

$$C = \mathbb{E}\left[AA^T\right], \qquad A = [a_2, a_3, \ldots, a_N]^T. \tag{39}$$

The method then applies a Cholesky factorization,

$$C = UU^T, \tag{40}$$

and draws a standard Gaussian vector $B \sim \mathcal{N}(0, I)$. The correlated Zernike coefficients are obtained by

$$A = UB. \tag{41}$$

This can also be read as a Karhunen-Loeve (K-L) expansion. Substituting Eq. (41) into the phase expansion gives

$$\boxed{\phi(\boldsymbol{\rho}) = Z(\boldsymbol{\rho})UB = \sum_{i=1}^{N-1} b_i K_i(\boldsymbol{\rho}),} \tag{42}$$

where each K_i is a linear combination of Zernike modes. While these Cholesky-built modes are not strictly orthogonal K-L modes in a mathematical sense, they provide a major computational advantage by drawing independent b_i successfully reproduces the desired atmospheric covariance in A [21]. This transformation defines the mode-correlated basis used by the methodology.

3.3 Generated Phase Screens and Validation

Using the described methodology, we generate phase screens as illustrated in Figure 2, where the grayscale gradient indicates the phase shift (ranging from 0 to 2π) applied to the light passing through each pixel. As Fried's parameter r_0 increases from the left figure to right, the strength of the atmospheric turbulence decreases, resulting in visibly smoother phase wavefronts. Other examples of generated phase screens are displayed in Appendix C.

To ensure the physical accuracy of the simulations, the numerically generated phase screens must be validated against theoretical atmospheric models. Given that the screen generation relies on a finite basis of Zernike polynomials, this validation confirms that the discrete numerical approach successfully reproduces the continuous spatial statistics of real turbulence. Specifically, we evaluate the phase structure function, which quantifies the expected phase variance between two points separated by a transverse distance vector $\boldsymbol{\rho}$. For an ensemble of generated screens, this empirical structure function is defined as:

$$D_\phi(\boldsymbol{\rho}) = \left\langle |\phi(\mathbf{x} + \boldsymbol{\rho}) - \phi(\mathbf{x})|^2 \right\rangle. \tag{43}$$

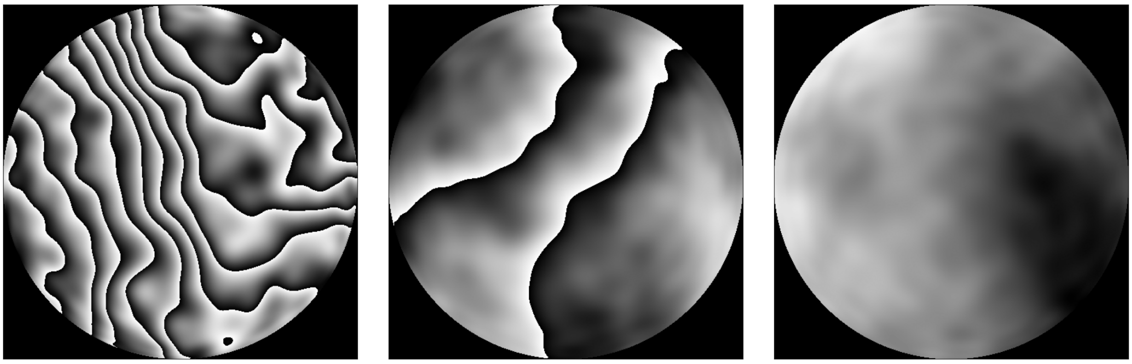

(a) $r_0 = 0.1$ cm (b) $r_0 = 0.5$ cm (c) $r_0 = 1$ cm

Figure 2: Comparison of the representation of atmospheric phase screens using the modified von Kármán model for different values of Fried's parameter (r_0). All screens are generated with a fixed aperture diameter $D = 2$ cm, outer scale $L_0 = 10$ m, and inner scale $l_0 = 1$ mm.

This average is then compared to the theoretical baseline of the chosen turbulence model. If the atmosphere is modeled using Kolmogorov statistics, the generated screens should follow the structure function:

$$D_{\mathrm{Kol}}(\boldsymbol{\rho}) = 6.88 \left| \frac{\rho}{r_0} \right|^{5/3}. \tag{44}$$

Alternatively, for the modified von Kármán model, the simulated screens are validated against the following algebraic approximation, which is valid in the spatial regimes where $\rho \ll l_0$ or $l_0 \ll \rho \ll L_0$ [27]:

$$D_{\mathrm{mvK}}(\boldsymbol{\rho}) \approx 7.754\, r_0^{-5/3} l_0^{-1/3} |\rho|^2 \left[\left(1 + 2.033 \left| \frac{\rho}{l_0} \right|^2 \right)^{-1/6} - 1.319 \left(\frac{l_0}{L_0} \right)^{1/3} \right]. \tag{45}$$

For the validation of the temporal spectra the covariance of the generated $G_{b,i}$ are compared with the theoretical values they should follow, indicated by the diagonal of the covariance matrix for each Zernike's j-th order. It is also verified that the normalized temporal spectra of different j-th orders follow a $\nu^{-17/3}$ asymptote at high-frequencies, for which the cutoff frequency is higher at higher j-th orders.

4 Modeling of Atmospheric Turbulence Effect on the Two Qubit Spatial Correlations

4.1 Concurrence model

With the framework established for generating phase screens that simulate the phase shifts experienced by light in a turbulent atmosphere, we can now simulate these effects on spatial correlations. By selecting two arbitrary alternative paths for the signal and idler photons, we calculate μ_{turb} as defined in Eq. (28). Averaging this over an ensemble of generated phase masks for various values of Fried's parameter r_0 allows us to characterize the impact of turbulence on two photon spatial correlations via their concurrence.

Because we assume a plane wave for the atmospheric models, we must apply the same plane wave wavefront for our two photon system. Consequently, the phase independent cross spectral density function is given by $\sqrt{S^{(2)}(\boldsymbol{r}_{s1},\boldsymbol{r}_{i1})S^{(2)}(\boldsymbol{r}_{s2},\boldsymbol{r}_{i2})}$ [18]. Assuming identical geometric and detection rate conditions for all apertures and alternative paths, meaning $k_1 = k_2$ and $S^{(2)}(\boldsymbol{r}_{s1},\boldsymbol{r}_{i1}) = S^{(2)}(\boldsymbol{r}_{s2},\boldsymbol{r}_{i2})$, the expression for concurrence from Eq. (25) simplifies to:

$$\mathcal{C}(\Omega_{\text{tp}}) = |\mu_{\text{turb}}| = \left|\left\langle e^{-i[\phi(\boldsymbol{r}_{s1})-\phi(\boldsymbol{r}_{s2})+\phi(\boldsymbol{r}_{i1})-\phi(\boldsymbol{r}_{i2})]}\right\rangle\right| \tag{46}$$

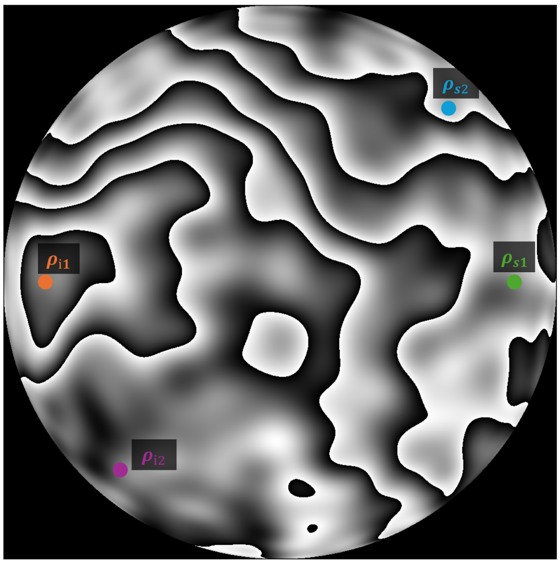

Figure 3: Example of transversal positions of signal and idler photons in two alternative paths at a generated phase screen.

Based on the setup described in Section 2.3, several geometric properties of the two qubit system provide useful physical insights. Using the transverse positions of the signal and idler photons for both alternative spatial modes at plane z, the position of the phase screen, as depicted in Figure 3. We then construct the following displacement parameters:

$$\boldsymbol{\rho}_1 = \frac{\boldsymbol{\rho}_{s1}+\boldsymbol{\rho}_{i1}}{2} \qquad \boldsymbol{\rho}_2 = \frac{\boldsymbol{\rho}_{s2}+\boldsymbol{\rho}_{i2}}{2} \qquad \Delta\boldsymbol{\rho} = \boldsymbol{\rho}_1 - \boldsymbol{\rho}_2$$
$$\boldsymbol{\rho}'_1 = \boldsymbol{\rho}_{s1} - \boldsymbol{\rho}_{i1} \qquad \boldsymbol{\rho}'_2 = \boldsymbol{\rho}_{s2} - \boldsymbol{\rho}_{i2} \qquad \Delta\boldsymbol{\rho}' = \boldsymbol{\rho}'_1 - \boldsymbol{\rho}'_2$$
$$\boldsymbol{d} = \frac{\boldsymbol{\rho}'_1+\boldsymbol{\rho}'_2}{2}.$$

By considering a Type I SPDC (detailed in Section 2.2) and by momentum conservation, the transverse position of the signal photon is opposite to the idler's ($\boldsymbol{\rho}_s = -\boldsymbol{\rho}_i$). Thus, the two photon transverse position vector difference is $\Delta\boldsymbol{\rho} = 0$. Meanwhile, the magnitude difference of the two photon asymmetry vectors, $\Delta\rho' = |\Delta\boldsymbol{\rho}'|$, describes the effective physical size of the two qubit system, and $d = |\boldsymbol{d}|$ represents the separation between the alternative apertures. Following the spatial mode convention $|\boldsymbol{\rho}'_1| > |\boldsymbol{\rho}'_2|$, we find that $d > \Delta\rho'/2$.

We can now derive theoretical expressions for the concurrence as a function of Fried's parameter r_0 to serve as a baseline for our simulation results. The detailed derivation is provided in Appendix B. These expressions rely on the spatial statistics of each model and take the form:

$$
\boxed{\begin{aligned}\mathcal{C}_{\mathcal{M}}(r_0) = \Bigg|\exp\Bigg\{-\frac{1}{2}\Bigg[2D_{\mathcal{M},r_0}\left(\frac{1}{2}\Delta\boldsymbol{\rho}'\right) + 2D_{\mathcal{M},r_0}\left(\boldsymbol{d}\right) \\ -D_{\mathcal{M},r_0}\left(\boldsymbol{d}+\frac{1}{2}\Delta\boldsymbol{\rho}'\right) - D_{\mathcal{M},r_0}\left(\boldsymbol{d}-\frac{1}{2}\Delta\boldsymbol{\rho}'\right)\Bigg]\Bigg\}\Bigg|\end{aligned}} \tag{47}
$$

where $D_{\mathcal{M},r_0}$ represents the phase structure function for the chosen model $\mathcal{M}$ (either Kolmogorov or modified von Kármán), which depends on r_0.

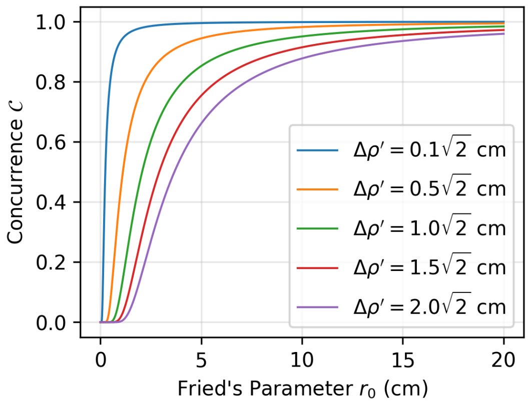

(a) Kolmogorov model with fixed $d = 2$ cm.

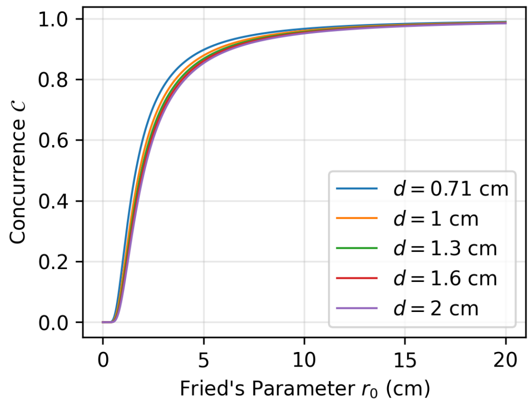

(b) Kolmogorov model with fixed $\Delta\rho' = 1.41$ cm.

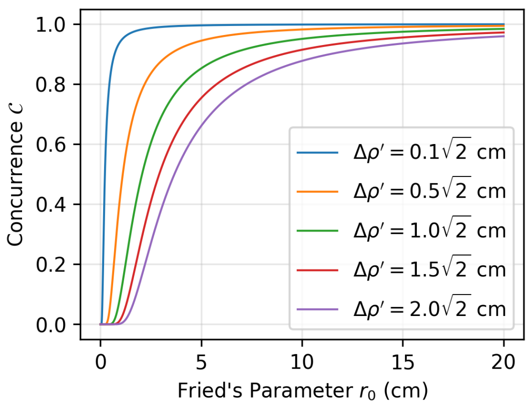

(c) von Kármán model with fixed $d = 2$ cm.

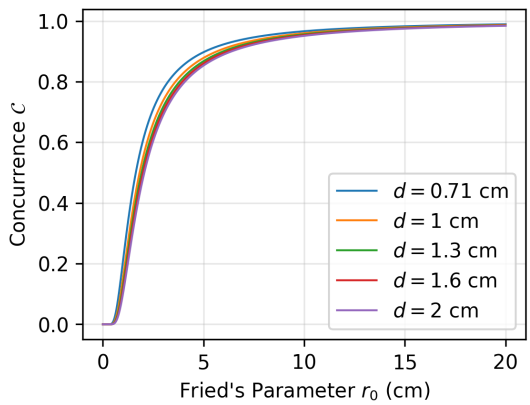

(d) von Kármán model with fixed $\Delta\rho' = 1.41$ cm.

Figure 4: Theoretical calculations for the concurrence ($\mathcal{C}$) of a two qubit system as a function of the Fried's Parameter (r_0) of the atmosphere. The top row (a, b) employs the Kolmogorov model, while the bottom row (c, d) uses the modified von Kármán model ($l_0 = 1$ mm, $L_0 = 10$ m). The left column shows concurrence for a fixed d with varying spatial separations $\Delta\rho'$, whereas the right column shows a fixed $\Delta\rho'$ with varying d. The values for d and $\Delta\rho'$ are representative values for the unit circle of the system's aperture (considered to be 2 cm).

Figure 4 shows the theoretical model values for concurrence of the two qubits in different atmospheric turbulence scenarios characterized by r_0. The physical description of the two photon system is also modified to better understand its effect on the spatial correlation's resistance to atmospheric turbulence. The left panels of the figure show that for a fixed value of d, increasing the effective spatial size $\Delta\rho'$ of the two photon system shifts the concurrence curve toward larger values of r_0. Therefore, larger spatial separations require weaker turbulence in order to preserve the same amount of entanglement. This effect is in line with the understanding of the Fried parameter as the diameter of the area where the light remains undisturbed when traveling through the atmosphere, since having the two photons closer together means that the spatial coherence is better maintained.

The right panel of Figure 4 show the complementary case of varying the separation parameter d when $\Delta\rho'$ is fixed. In comparison to the effect of the previous parameter, the influence of d is much weaker, as the curves remains closer to each other for all turbulence strengths considered. This shows that the concurrence degradation is mainly controlled by the effective physical size of the correlated two photon state rather than the absolute separation between the two alternative apertures.

Another relevant observation from Figure 4 is that both theoretical models for concurrence based on Kolmogorov and modified von Kármán atmospheric models yield the same results. This is not immediately obvious from the theoretical expressions derived for each, since their respective phase structure functions differ from each other. However, the difference between models starts to reveal itself when the effective physical size of the two photon system $\Delta\rho'$ is small enough to compare with the inner scale l_0 selected for the modified von Kármán structure, but that effect arises from the assumptions made in the model.

4.2 Numerical Procedure and Results

As previously mentioned, the method employed for estimating concurrence involves averaging the computation of μ_{turb} over an ensemble of phase screens generated from specific atmospheric parameters. The steps followed to achieve this can be summarized as follows:

1. Two arbitrary positions are defined for the alternative transverse paths of the signal photon inside the aperture; the corresponding alternative paths for the idler photon are then set opposite to their respective signal position. The relevant displacement parameters $\boldsymbol{\Delta\rho'}$ and $\boldsymbol{d}$ are obtained and used to compute the theoretical function for the concurrence.

2. The phase screen is generated using the developed framework, based on the respective atmospheric parameters of the chosen the model. In the Kolmogorov model, these parameters are the system aperture D and Fried's parameter r_0, while the modified von Kármán model additionally considers the inner l_0 and outer L_0 scales. For each screen generation, 500 Zernike polynomials were employed, as previous studies have shown that this number of terms produces accurate simulation results [17].

3. Once the static phase screen is generated, the phase shift values at the four defined positions are extracted, and the exponential term from Eq. (28) is computed. Then, a new phase screen with identical parameters is generated. Due to the stochastic process employed in the framework, this screen is statistically independent from the previous one, so a new value for the exponential term is computed. This process is repeated 1000 times, allowing μ_{turb} to be calculated as the ensemble average of these values.

4. Concurrence is then the absolute value of this resulting average, with its standard deviation used as a measure of uncertainty. Because each simulated concurrence value corresponds to a single r_0 point, an adaptive sample algorithm was utilized to efficiently sample the parameter space. This algorithm specifically selected the Fried's parameter values in regions where the concurrence presented the most rapid changes. This method is described in more detail in Appendix D.

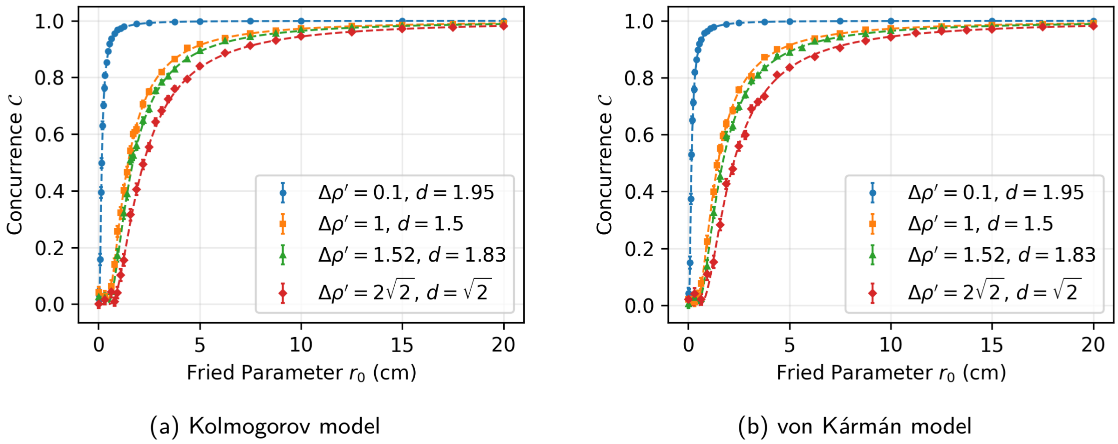

Figure 5: Comparison of the concurrence $\mathcal{C}$ as a function of the Fried parameter r_0 for various spatial configurations (defined by spatial separation $\Delta\rho'$ and effective diameter d). The left panel (a) shows the results using the Kolmogorov turbulence model, while the right panel (b) shows the modified von Kármán model. Dashed lines represent the theoretical calculations, and markers with error bars indicate the corresponding numerical simulation results.

Figure 5 presents the results of the simulations for different positions of the signal and idler photons that yield different displacement parameters. The simulation results agree with the theoretical models both for Kolmogorov and modified von Kármán. There is, however, a slight error in the simulation values at very low values of Fried's parameter. This can be explained from Eq. (46) that takes the absolute value of the μ_{turb} averages, so it tends to average over zero. An individual of the results is shown in Appendix E.

Figures 4 and 5 show the dependence of the concurrence on Fried's parameter r_0 for different spatial configurations of the two photon system. Since r_0 represents the coherence length of the turbulent wavefront, small values of r_0 correspond to strong turbulence, while larger values correspond to weaker phase distortions. In all cases, the concurrence tends to zero for sufficiently strong turbulence and approaches one as the Fried's parameter increases. What this means physically is that spatial entanglement is degraded when the turbulent phase varies significantly across the transverse positions of the two alternatives of the biphoton state, while it is preserved when the turbulent medium is approximately coherent over that region.

Overall, these results show that the atmospheric turbulence can strongly degrade spatial entanglement when the size of the two photon state is large compared with the coherence length r_0. For free space quantum communications, this implies that spatially encoded entangled states are more robust when their relevant spatial components remain within a region of closely correlated atmospheric phase. On the other side, spatial modes with larger transverse extension or wider separation are expected to be more sensitive to turbulence induced decoherence, which may require optimized spatial encoding, adaptive optics or turbulence compensation.

At the same time, the agreement between the numerical simulations and the theoretical curves shows that the phase screen generation methodology accurately reproduces the spatial entanglement statistics for a bipartite quantum system consisting on two correlated photons generated through Type I SPDC. However, the phase screen analysis is not limited by the simplifications and assumptions made for the theoretical derivations. Instead, this methodology and framework may be applied to study any spatial entanglement between different spatial bases, other SPDC configurations and higher dimensional or multipartite quantum states.

5 Conclusions and Further Work

The present work studied the effect of atmospheric turbulence on the spatial entanglement of photon pairs generated through spontaneous parametric down-conversion. The main objective was to go beyond a description of turbulence as a simple optical loss mechanism and analyze how random phase distortions affect the spatial coherence terms that determine the concurrence of a two photon spatial qubit state. In this sense, this work connects the spatial correlations produced by SPDC, the description of atmospheric turbulence through statistical phase models, and the quantification of entanglement through concurrence.

A first result of this thesis is the theoretical formulation of the turbulence induced reduction of concurrence for spatial two-qubit states for both Kolmogorov and modified von Kármán descriptions. By modeling the atmosphere as a stochastic phase screen, the effect of turbulence can be expressed through an ensemble average of phase differences evaluated at the four transverse positions that define the two spatial alternatives of the biphoton state. This leads to a compact expression that relates atmospheric phase statistics to the loss of coherence. The theoretical expression for both models is an useful basis for predicting how concurrence depends on Fried's parameter r_0, the effective size of the two photon state and the separation between spatial modes.

The numerical results show that the degradation of concurrence is principally influenced by the relation between the characteristic transverse dimensions of the biphoton system and the atmospheric coherence length represented by r_0. When the spatial modes are kept within a region over which the turbulent wavefront remains approximately coherent, concurrence is mostly preserved. In contrast, when the relevant spatial separations become comparable to or larger than r_0, the random phase fluctuations reduce the coherence between the alternatives and so the entanglement decreases.

Another important contribution of this work is the implementation of a phase screen generation framework based on Zernike polynomials. Some open source tools for atmospheric phase screen generation, such as WavePy and MegaScreen are already available and provide useful references for turbulence simulation. However these tools are generally based on spectral or multiscale synthesis methods, centered on Kolmogorov statistics. In contrast, the framework developed in this thesis follows a modal approach, in which the turbulent phase is decomposed into Zernike modes and generated from coefficients with covariance determined by the selected atmospheric model. This allows the method to incorporate both Kolmogorov and modified von Kármán statistics. The framework is not restricted to the specific two qubit concurrence calculation considered in this thesis, but can also be used as a general tool for simulating atmospheric propagation in classical and quantum optical systems.

Furthermore, the extension of the framework to dynamic phase screens adds to its usefulness. Although dynamic ensemble averages lead to the same concurrence behavior as static phase screens under the assumptions used in this work, the dynamic model is important for propagation in time-dependent studies, experimental setups with spatial light modulators, adaptive optics corrections and realistic communication scenarios in which the channel evolves in time. Therefore, the dynamic phase screen generator method developed here should be seen as a broader simulation tool, even if the main entanglement analysis of this thesis focuses on averaged spatial coherence.

From the quantum information perspective, the framework developed in this work provides a basis for studying atmospheric effects on more general spatial quantum correlations. The two qubit model considered here is an useful minimal system because it makes the connection between spatial coherence and concurrence explicit. However, the same methodology can be extended to more complex spatial encodings, including higher dimension qudits, orbital angular momentum modes and other spatial modes bases. This is particularly relevant for free-space quantum communication since high dimensional spatial encoding can increase the information capacity of a quantum channel and may be useful in protocols such as high dimensional quantum key distribution and dense coding.

In fact, the study of the effect of turbulence higher dimension spatial states is one of the many open directions for future work. Studying not only concurrence, but also other entanglement measures and quality of channel metrics would allow a more direct comparison between different spatial encodings to identify which modal bases are more robust under realistic atmospheric conditions for different use cases and applications.

A potential extension of this work would be the experimental implementation of the model. The generated phase screens, both static and dynamic, can be displayed on a spatial light modulator to emulate controlled atmospheric turbulence in the laboratory. This would allow direct experimental validation of the predicted concurrence degradation and would also make it possible to test mitigation strategies, such as adaptive optics, optimized spatial mode selection or turbulence aware encoding schemes.

Another possible direction is to study in more detail the extension of the relation between turbulence and entanglement. In particular, this framework could be further explored in contexts such as quantum metrology, where spatially entangled photons may provide useful information about atmospheric turbulence.

Finally, the atmospheric simulation framework has potential applications outside specific quantum scenario considered here. Since the generated phase screens reproduce regular turbulence statistics, they are also useful for classical free-space optical communication, imaging through turbulence, beam propagation studies and adaptive optics simulations. In this sense, the work developed in this thesis contributes not only to the study of spatial entanglement under atmospheric turbulence, but also to the general modeling of wavefront propagation through turbulent media.

References

[1] C. H. Bennett and G. Brassard, "Quantum cryptography: Public key distribution and coin tossing," in *Proceedings of the IEEE International Conference on Computers, Systems and Signal Processing*, (Bangalore, India), pp. 175–179, 1984.

[2] V. Scarani, H. Bechmann-Pasquinucci, N. J. Cerf, M. Dusek, N. Lutkenhaus, and M. Peev, "The security of practical quantum key distribution," vol. 81, no. 3, pp. 1301–1350.

[3] D. Alvarez and Y. Kim, "Survey of the development of quantum cryptography and its applications," in *2021 IEEE 11th Annual Computing and Communication Workshop and Conference (CCWC)*, pp. 1074–1080, IEEE.

[4] J. S. Sidhu, S. K. Joshi, M. Gündoğan, T. Brougham, D. Lowndes, L. Mazzarella, M. Krutzik, S. Mohapatra, D. Dequal, G. Vallone, P. Villoresi, A. Ling, T. Jennewein, M. Mohageg, J. G. Rarity, I. Fuentes, S. Pirandola, and D. K. L. Oi, "Advances in space quantum communications," *IET Quantum Communication*, vol. 2, no. 4, p. 182–217, 2021.

[5] J. Jordan-Parra, M. Garcia-Romero, J. Gil-Lopez, J. A. Ruiz-De-Azua, and J. Paradells, "Satellite quantum key distribution: Analysis, modeling, performance evaluation, and validation," vol. 6, pp. 8241–8271.

[6] J. W. Goodman, *Statistical Optics*. John Wiley & Sons, 2015.

[7] M. Malik, M. O'Sullivan, B. Rodenburg, M. Mirhosseini, J. Leach, M. P. J. Lavery, M. J. Padgett, and R. W. Boyd, "Influence of atmospheric turbulence on optical communications using orbital angular momentum for encoding," vol. 20, no. 12, p. 13195.

[8] R. Shekel, O. Lib, A. Sardas, and Y. Bromberg, "Shaping entangled photons through emulated turbulent atmosphere," vol. 4, no. 8, p. 2339.

[9] N. J. Cerf, M. Bourennane, A. Karlsson, and N. Gisin, "Security of quantum key distribution using d-level systems," *Physical Review Letters*, vol. 88, Mar. 2002.

[10] S. Gröblacher, T. Jennewein, A. Vaziri, G. Weihs, and A. Zeilinger, "Experimental quantum cryptography with qutrits," *New Journal of Physics*, vol. 8, p. 75, may 2006.

[11] C. H. Monken, P. H. S. Ribeiro, and S. Pádua, "Transfer of angular spectrum and image formation in spontaneous parametric down-conversion," *Physical Review A*, vol. 57, no. 4, pp. 3123–3126, 1998.

[12] S. P. Walborn, C. H. Monken, S. Pádua, and P. H. S. Ribeiro, "Spatial correlations in parametric down-conversion," *Physics Reports*, vol. 495, pp. 87–139, 2010.

[13] J. Schneeloch and J. C. Howell, "Introduction to the transverse spatial correlations in spontaneous parametric down-conversion through the biphoton birth zone," *Journal of Optics*, vol. 18, no. 5, p. 053501, 2016.

[14] A. K. Jha and R. W. Boyd, "Spatial two-photon coherence of the entangled field produced by down-conversion using a partially spatially coherent pump beam," *Physical Review A*, vol. 81, 2010.

[15] S. Hill and W. K. Wootters, "Entanglement of a pair of quantum bits," *Physical Review Letters*, vol. 78, no. 26, pp. 5022–5025, 1997.

[16] W. K. Wootters, "Entanglement of formation of an arbitrary state of two qubits," *Physical Review Letters*, vol. 80, no. 10, pp. 2245–2248, 1998.

[17] N. A. Roddier, "Atmospheric wavefront simulation using Zernike polynomials," vol. 29, no. 10, p. 1174.

[18] A. K. Jha, G. A. Tyler, and R. W. Boyd, "Effects of atmospheric turbulence on the entanglement of spatial two-qubit states," *Physical Review A*, vol. 81, 2010.

[19] D. L. Fried, "Statistics of a geometric representation of wavefront distortion," vol. 55, no. 11, p. 1427.

[20] R. J. Noll, "Zernike polynomials and atmospheric turbulence," vol. 66, no. 3, p. 207.

[21] B. Lu and D. Cai, "Simulation of a temporally dynamic atmospheric wavefront using the modified von-Kármán spectrum and Zernike-based method," vol. 32, no. 22, p. 38609.

[22] R. J. Glauber, "The quantum theory of optical coherence," *Physical Review*, vol. 130, no. 6, pp. 2529–2539, 1963.

[23] B. Baghdasaryan, C. Sevilla-Gutiérrez, F. Steinlechner, and S. Fritzsche, "Generalized description of the spatio-temporal biphoton state in spontaneous parametric down-conversion," *Physical Review A*, vol. 106, no. 6, p. 063711, 2022.

[24] M. W. Mitchell, *Quantum Optics for the Impatient.* ICFO - Institut de Ciencies Fotoniques, 2021. Version 1.6.

[25] R. W. Boyd, ed., *Nonlinear optics.* Academic Press, third ed.

[26] P. W. Milonni, "Resource letter: Aoa-1: adaptive optics for astronomy," *American Journal of Physics*, vol. 67, no. 6, pp. 476–485, 1999.

[27] L. Andrews, S. Vester, and C. Richardson, "Analytic expressions for the wave structure function based on a bump spectral model for refractive index fluctuations," *Journal of Modern Optics*, vol. 40, no. 5, pp. 931–938, 1993.

[28] D. L. Fried, "Optical resolution through a randomly inhomogeneous medium for very long and very short exposures," *Journal of the Optical Society of America*, vol. 56, no. 10, pp. 1372–1379, 1966.

[29] R. G. Lane, A. Glindemann, and J. C. Dainty, "Simulation of a kolmogorov phase screen," vol. 2, no. 3, pp. 209–224.

[30] Y. Li, B. Lu, H. Xue, N. Wang, and D. Cai, "Fast and robust simulation of atmospheric phase screen by Zernike polynomials with recursive radial formulas," vol. 7, no. 4, p. 58.

[31] J.-M. Conan, G. Rousset, and P.-Y. Madec, "Wave-front temporal spectra in high-resolution imaging through turbulence," vol. 12, no. 7, p. 1559.

[32] E. Anzuola and S. Gladysz, "Modeling dynamic atmospheric turbulence using temporal spectra and karhunen–loève decomposition," vol. 56, no. 7, p. 1.

[33] C. C. Wilcox, "Performance of a flexible optical aberration generator," vol. 50, no. 11, p. 116601.

[34] I. B. Putnam and S. C. Cain, "Modeling a temporally evolving atmosphere with Zernike polynomials," 2012.

[35] L. Burger, I. A. Litvin, and A. Forbes, "Simulating atmospheric turbulence using a phase-only spatial light modulator,"

A Dynamic Screens

For a time-dependent atmosphere, the coefficients of the Zernike polynomials become functions of time:

$$\phi(\boldsymbol{\rho}, t) = \sum_{j=2}^{N} G_{a,j}(t) Z_j(\rho, \theta). \tag{48}$$

The objective is that each $G_{a,j}(t)$ has a zero mean, the correct variance C_{jj}, and the correct temporal power spectrum $w_{a,j}(\nu)$. The temporal part follows Conan's derivation of wavefront temporal spectra and the inverse-Fourier sampling method used by Anzuola and Gladysz [31, 32]. Wilcox et al. and Putnam and Cain are useful context for earlier time-evolving Zernike approaches, but this methodology follows the Lu and Cai spectral route [33, 34, 21].

The link between spatial and temporal spectra is Taylor's frozen-flow hypothesis:

$$\phi(\boldsymbol{\rho}, t + \tau) = \phi(\boldsymbol{\rho} - \mathbf{V}\tau, t), \tag{49}$$

which states that during a short time interval τ, the turbulent phase pattern is assumed to remain unchanged and is transported by a wind velocity $\mathbf{V}$. Thus, the wind velocity controls the speed of the temporal fluctuations, as larger values shift the model spectra towards higher temporal frequencies. Meanwhile, the turbulence strength determines the variance of each coeffiecient.

For the simple homogeneous plane-wave case, with one layer moving along the x axis at speed V, the temporal spectrum is

$$w_{a,j}(\nu) = \frac{LC_n^2}{V} F_{a,j}\left(\frac{\nu}{V}, L_0, l_0\right), \tag{50}$$

where

$$\begin{aligned} F_{a,j}(k_x, L_0, l_0) = 0.00969 \left(\frac{2\pi}{\lambda}\right)^2 \int_{-\infty}^{\infty} &|Q_j(k_x, k_y)|^2 \\ &\times \frac{\exp\left[-\left(\frac{2\pi l_0}{5.92}\right)^2 (k_x^2 + k_y^2)\right]}{\left(k_x^2 + k_y^2 + L_0^{-2}\right)^{11/6}} dk_y. \end{aligned} \tag{51}$$

Q_j is the Fourier transform of the pupil-weighted Zernike mode, whose radial dependence is

$$Q_j(k_x, k_y) \propto \sqrt{n+1} \frac{J_{n+1}(2\pi Rk)}{\pi Rk}, \qquad k = \sqrt{k_x^2 + k_y^2}, \tag{52}$$

plus the cosine or sine angular factor for $m \neq 0$. The numerical integral in Eq. (51) is even in k_y, so it can be evaluated from 0 to ∞ and doubled.

Wind direction can be added without recomputing the full two-dimensional problem for every angle. If the wind makes an angle θ_w with the x axis, Conan's result used by Lu and Cai gives, for $m \neq 0$,

$$w_{a,j,\theta_w}(\nu) = \cos^2(m\theta_w)\, w_{a,j,0}(\nu) + \sin^2(m\theta_w)\, w_{a,j^-,0}(\nu), \tag{53}$$

where j^- is the Zernike mode with the same (n, m) but opposite sine/cosine parity. Modes with $m = 0$ are rotationally symmetric, so their spectra do not depend on wind direction.

For a multi-layer atmosphere, the total temporal spectrum is a sum of the contribution from each layer. For layer q, with thickness Δz_q, representative altitude z_q, wind speed V_q, wind direction θ_q, turbulence strength $C_{n,q}^2$, and scales $L_{0,q}$ and $l_{0,q}$, the plane/spherical-wave form can be written as

$$w_{a,j}(\nu) = \sum_{q=1}^{Q} \frac{\Delta z_q C_{n,q}^2}{V_q} \left(1 - \frac{z_q}{L}\right)^{\frac{8}{3}\delta_{\mathrm{sp}}} F_{a,j,\theta_q}\left(\frac{\nu}{V_q}\left(1 - \frac{z_q}{L}\right)^{\delta_{\mathrm{sp}}}, L_{0,q}, l_{0,q}\right). \tag{54}$$

For the plane-wave case, $\delta_{\mathrm{sp}} = 0$, so the extra spherical-wave factors disappear and each layer simply adds a weighted spectrum. This expression provides the natural extension for adding a wind profile and several turbulent slabs.

After computing $w_{a,j}(\nu)$ on the FFT frequency grid, the time sequence is generated by filtering random Fourier coefficients:

$$\widehat{G}_{a,j}(\nu_k) = \sqrt{w_{a,j}(\nu_k)}\exp(i\psi_k), \qquad \psi_k \sim U(0, 2\pi). \tag{55}$$

The inverse real FFT gives a time series $G_{a,j}(t)$. The series is then centered and rescaled so that its standard deviation matches $\sqrt{C_{jj}}$. If these sequences were inserted directly into Eq. (48), the spatial covariance would become diagonal because every modal time sequence was drawn independently. The procedure used by Lu and Cai is to normalize the time sequences and apply them to the Cholesky-built modes:

$$G_{b,i}(t) = \frac{G_{a,i+1}(t)}{\sqrt{C_{i+1,i+1}}}, \tag{56}$$

$$\phi(\boldsymbol{\rho}, t) = \sum_{i=1}^{N-1} G_{b,i}(t) K_i(\boldsymbol{\rho}). \tag{57}$$

This gives screens that keep the spatial covariance imposed by Eq. (37), while their time evolution follows the temporal spectra from Eq. (50) or the multi-layer extension in Eq. (54). The simulated phase is finally wrapped modulo 2π and converted to an 8-bit grayscale image for the phase-only SLM [35].

B Derivation of a Theoretical Expression for Concurrence in Kolmogorov and modified von Kármán models

Since for our methodology we employ random Gaussian variables for generating the phase screens, we may apply the standard result $\langle e^{-i\varphi} \rangle = e^{-\frac{1}{2}\langle \varphi^2 \rangle}$ to Eq. (46) so that:

$$
\begin{aligned}
\varphi^2 &= [\phi(\mathbf{r}_{s1}) - \phi(\mathbf{r}_{s2}) + \phi(\mathbf{r}_{i1}) - \phi(\mathbf{r}_{i2})]^2 \\
&= \phi^2(\mathbf{r}_{s1}) - \phi(\mathbf{r}_{s1})\phi(\mathbf{r}_{s2}) + \phi(\mathbf{r}_{s1})\phi(\mathbf{r}_{i1}) - \phi(\mathbf{r}_{s1})\phi(\mathbf{r}_{i2}) \\
&\quad - \phi(\mathbf{r}_{s1})\phi(\mathbf{r}_{s2}) + \phi^2(\mathbf{r}_{s2}) - \phi(\mathbf{r}_{s2})\phi(\mathbf{r}_{i1}) + \phi(\mathbf{r}_{s2})\phi(\mathbf{r}_{i2}) \\
&\quad + \phi(\mathbf{r}_{s1})\phi(\mathbf{r}_{i1}) - \phi(\mathbf{r}_{s2})\phi(\mathbf{r}_{i1}) + \phi^2(\mathbf{r}_{i1}) - \phi(\mathbf{r}_{i1})\phi(\mathbf{r}_{i2}) \\
&\quad - \phi(\mathbf{r}_{s1})\phi(\mathbf{r}_{i2}) + \phi(\mathbf{r}_{s2})\phi(\mathbf{r}_{i2}) - \phi(\mathbf{r}_{i1})\phi(\mathbf{r}_{i2}) + \phi^2(\mathbf{r}_{i2}) \\
&= [\phi(\mathbf{r}_{s1}) - \phi(\mathbf{r}_{s2})]^2 + [\phi(\mathbf{r}_{i1}) - \phi(\mathbf{r}_{i2})]^2 \\
&\quad + 2\phi(\mathbf{r}_{s1})\phi(\mathbf{r}_{i1}) - \phi^2(\mathbf{r}_{s1}) - \phi^2(\mathbf{r}_{i1}) \\
&\quad - 2\phi(\mathbf{r}_{s1})\phi(\mathbf{r}_{i2}) + \phi^2(\mathbf{r}_{s1}) + \phi^2(\mathbf{r}_{i2}) \\
&\quad - 2\phi(\mathbf{r}_{s2})\phi(\mathbf{r}_{i1}) + \phi^2(\mathbf{r}_{s2}) + \phi^2(\mathbf{r}_{i1}) \\
&\quad + 2\phi(\mathbf{r}_{s2})\phi(\mathbf{r}_{i2}) - \phi^2(\mathbf{r}_{s2}) - \phi^2(\mathbf{r}_{i2}) \\
&= [\phi(\mathbf{r}_{s1}) - \phi(\mathbf{r}_{s2})]^2 + [\phi(\mathbf{r}_{i1}) - \phi(\mathbf{r}_{i2})]^2 \\
&\quad - [\phi(\mathbf{r}_{s1}) - \phi(\mathbf{r}_{i1})]^2 + [\phi(\mathbf{r}_{s1}) - \phi(\mathbf{r}_{i2})]^2 \\
&\quad + [\phi(\mathbf{r}_{s2}) - \phi(\mathbf{r}_{i1})]^2 - [\phi(\mathbf{r}_{s2}) - \phi(\mathbf{r}_{i2})]^2 .
\end{aligned}
$$

It is then evident that the expected value of this expression consists of the sum of the phase structure function evaluated at different transversal positions at plane z.

B.1 Kolmogorov

Applying the Kolmogorov phase structure function

$$
\left\langle [\phi(\boldsymbol{\rho}_a) - \phi(\boldsymbol{\rho}_b)]^2 \right\rangle_{\text{Kol}} = 6.88 \left| \frac{\boldsymbol{\rho}_a - \boldsymbol{\rho}_b}{r_0} \right|^{5/3},
$$

to the expression obtained above gives

$$
\begin{aligned}
\left\langle \varphi^2 \right\rangle_{\text{Kol}} = \frac{6.88}{r_0^{5/3}} \Big[&|\boldsymbol{\rho}_{s1} - \boldsymbol{\rho}_{s2}|^{5/3} + |\boldsymbol{\rho}_{i1} - \boldsymbol{\rho}_{i2}|^{5/3} - |\boldsymbol{\rho}_{s1} - \boldsymbol{\rho}_{i1}|^{5/3} \\
&+ |\boldsymbol{\rho}_{s1} - \boldsymbol{\rho}_{i2}|^{5/3} + |\boldsymbol{\rho}_{s2} - \boldsymbol{\rho}_{i1}|^{5/3} - |\boldsymbol{\rho}_{s2} - \boldsymbol{\rho}_{i2}|^{5/3} \Big].
\end{aligned}
$$

In terms of the displacement parameters

$$
\begin{cases}
\boldsymbol{\rho}_1 = \dfrac{\boldsymbol{\rho}_{s1} + \boldsymbol{\rho}_{i1}}{2}, \\
\boldsymbol{\rho}_2 = \dfrac{\boldsymbol{\rho}_{s2} + \boldsymbol{\rho}_{i2}}{2}, \\
\Delta\boldsymbol{\rho} = \boldsymbol{\rho}_1 - \boldsymbol{\rho}_2 = \dfrac{1}{2} [\boldsymbol{\rho}_{s1} - \boldsymbol{\rho}_{s2} + \boldsymbol{\rho}_{i1} - \boldsymbol{\rho}_{i2}], \\
\boldsymbol{\rho}'_1 = \boldsymbol{\rho}_{s1} - \boldsymbol{\rho}_{i1}, \\
\boldsymbol{\rho}'_2 = \boldsymbol{\rho}_{s2} - \boldsymbol{\rho}_{i2}, \\
\Delta\boldsymbol{\rho}' = \boldsymbol{\rho}'_1 - \boldsymbol{\rho}'_2 = \boldsymbol{\rho}_{s1} - \boldsymbol{\rho}_{s2} - \boldsymbol{\rho}_{i1} + \boldsymbol{\rho}_{i2}, \\
\boldsymbol{d} = \dfrac{\boldsymbol{\rho}'_1 + \boldsymbol{\rho}'_2}{2} = \dfrac{1}{2} [\boldsymbol{\rho}_{s1} + \boldsymbol{\rho}_{s2} - (\boldsymbol{\rho}_{i1} + \boldsymbol{\rho}_{i2})],
\end{cases}
$$

the relevant separations are

$$\begin{cases} \boldsymbol{\rho}_{s1} - \boldsymbol{\rho}_{s2} = \Delta\boldsymbol{\rho} + \frac{1}{2}\Delta\boldsymbol{\rho}', \\ \boldsymbol{\rho}_{i1} - \boldsymbol{\rho}_{i2} = \Delta\boldsymbol{\rho} - \frac{1}{2}\Delta\boldsymbol{\rho}', \\ \boldsymbol{\rho}_{s1} - \boldsymbol{\rho}_{i1} = \boldsymbol{d} + \frac{1}{2}\Delta\boldsymbol{\rho}', \\ \boldsymbol{\rho}_{s1} - \boldsymbol{\rho}_{i2} = \boldsymbol{d} + \Delta\boldsymbol{\rho}, \\ \boldsymbol{\rho}_{s2} - \boldsymbol{\rho}_{i1} = \boldsymbol{d} - \Delta\boldsymbol{\rho}, \\ \boldsymbol{\rho}_{s2} - \boldsymbol{\rho}_{i2} = \boldsymbol{d} - \frac{1}{2}\Delta\boldsymbol{\rho}'. \end{cases}$$

Therefore,

$$\begin{aligned} \left\langle \varphi^2 \right\rangle_{\mathrm{Kol}} = \frac{6.88}{r_0^{5/3}} \Bigg[& \left|\Delta\boldsymbol{\rho} + \frac{1}{2}\Delta\boldsymbol{\rho}'\right|^{5/3} + \left|\Delta\boldsymbol{\rho} - \frac{1}{2}\Delta\boldsymbol{\rho}'\right|^{5/3} \\ & - \left|\boldsymbol{d} + \frac{1}{2}\Delta\boldsymbol{\rho}'\right|^{5/3} + |\boldsymbol{d} + \Delta\boldsymbol{\rho}|^{5/3} + |\boldsymbol{d} - \Delta\boldsymbol{\rho}|^{5/3} \\ & - \left|\boldsymbol{d} - \frac{1}{2}\Delta\boldsymbol{\rho}'\right|^{5/3} \Bigg]. \end{aligned}$$

For type-I SPDC, $\Delta\boldsymbol{\rho} = 0$. Thus,

$$\left\langle \varphi^2 \right\rangle_{\mathrm{Kol}} = \frac{6.88}{r_0^{5/3}} \left[2\left|\frac{1}{2}\Delta\boldsymbol{\rho}'\right|^{5/3} + 2|\boldsymbol{d}|^{5/3} - \left|\boldsymbol{d} + \frac{1}{2}\Delta\boldsymbol{\rho}'\right|^{5/3} - \left|\boldsymbol{d} - \frac{1}{2}\Delta\boldsymbol{\rho}'\right|^{5/3} \right].$$

Therefore, since

$$\left\langle e^{-i\varphi} \right\rangle = \exp\left[-\frac{1}{2}\left\langle \varphi^2 \right\rangle\right],$$

the Kolmogorov turbulence factor is

$$\boxed{\mu_{\mathrm{turb,Kol}} = \exp\left\{ -\frac{3.44}{r_0^{5/3}} \left[2\left|\frac{1}{2}\Delta\boldsymbol{\rho}'\right|^{5/3} + 2|\boldsymbol{d}|^{5/3} - \left|\boldsymbol{d} + \frac{1}{2}\Delta\boldsymbol{\rho}'\right|^{5/3} - \left|\boldsymbol{d} - \frac{1}{2}\Delta\boldsymbol{\rho}'\right|^{5/3} \right] \right\}.}$$

Equivalently,

$$\boxed{\mu_{\mathrm{turb,Kol}} = \exp\left\{ -\frac{1}{2} \left[2D_{\mathrm{Kol}}\left(\frac{1}{2}\Delta\boldsymbol{\rho}'\right) + 2D_{\mathrm{Kol}}(\boldsymbol{d}) - D_{\mathrm{Kol}}\left(\boldsymbol{d} + \frac{1}{2}\Delta\boldsymbol{\rho}'\right) - D_{\mathrm{Kol}}\left(\boldsymbol{d} - \frac{1}{2}\Delta\boldsymbol{\rho}'\right) \right] \right\}.}$$

B.2 Modified von Kármán

For the modified von Kármán model, the phase structure function is

$$\left\langle [\phi(\boldsymbol{\rho}_a) - \phi(\boldsymbol{\rho}_b)]^2 \right\rangle_{\mathrm{mvK}} = \frac{7.754}{r_0^{5/3} L_0^{1/3}} |\boldsymbol{\rho}_a - \boldsymbol{\rho}_b|^2 \left[\left(1 + \frac{7.033}{L_0^2} |\boldsymbol{\rho}_a - \boldsymbol{\rho}_b|^2\right)^{-1/6} - 1.319 \left(\frac{\ell_0}{L_0}\right)^{1/3} \right],$$

where L_0 is the outer scale and ℓ_0 is the inner scale of turbulence.

Defining

$$\alpha = \frac{7.033}{L_0^2}, \qquad \beta = 1.319 \left(\frac{\ell_0}{L_0}\right)^{1/3},$$

and

$$F(\boldsymbol{x}) = |\boldsymbol{x}|^2 \left[\left(1 + \alpha|\boldsymbol{x}|^2\right)^{-1/6} - \beta \right],$$

we may write

$$D_{\text{mvK}}(\boldsymbol{x}) = \frac{7.754}{r_0^{5/3} L_0^{1/3}} F(\boldsymbol{x}).$$

Using the same displacement parameters as before, the expected phase variance is

$$\begin{aligned}
\left\langle \varphi^2 \right\rangle_{\text{mvK}} = \frac{7.754}{r_0^{5/3} L_0^{1/3}} \Bigg[& F\left(\Delta\boldsymbol{\rho} + \frac{1}{2}\Delta\boldsymbol{\rho}'\right) + F\left(\Delta\boldsymbol{\rho} - \frac{1}{2}\Delta\boldsymbol{\rho}'\right) \\
& - F\left(\boldsymbol{d} + \frac{1}{2}\Delta\boldsymbol{\rho}'\right) + F(\boldsymbol{d} + \Delta\boldsymbol{\rho}) + F(\boldsymbol{d} - \Delta\boldsymbol{\rho}) \\
& - F\left(\boldsymbol{d} - \frac{1}{2}\Delta\boldsymbol{\rho}'\right) \Bigg].
\end{aligned}$$

For type-I SPDC, $\Delta\boldsymbol{\rho} = 0$. Therefore,

$$\begin{aligned}
\left\langle \varphi^2 \right\rangle_{\text{mvK}} = \frac{7.754}{r_0^{5/3} L_0^{1/3}} \Bigg[& 2\left|\frac{1}{2}\Delta\boldsymbol{\rho}'\right|^2 \left[\left(1 + \alpha\left|\frac{1}{2}\Delta\boldsymbol{\rho}'\right|^2\right)^{-1/6} - \beta\right] \\
& + 2|\boldsymbol{d}|^2 \left[\left(1 + \alpha|\boldsymbol{d}|^2\right)^{-1/6} - \beta\right] \\
& - \left|\boldsymbol{d} + \frac{1}{2}\Delta\boldsymbol{\rho}'\right|^2 \left[\left(1 + \alpha\left|\boldsymbol{d} + \frac{1}{2}\Delta\boldsymbol{\rho}'\right|^2\right)^{-1/6} - \beta\right] \\
& - \left|\boldsymbol{d} - \frac{1}{2}\Delta\boldsymbol{\rho}'\right|^2 \left[\left(1 + \alpha\left|\boldsymbol{d} - \frac{1}{2}\Delta\boldsymbol{\rho}'\right|^2\right)^{-1/6} - \beta\right] \Bigg].
\end{aligned}$$

Finally, the modified von Kármán turbulence factor is

$$\boxed{\mu_{\text{turb,mvK}} = \exp\left\{ -\frac{3.877}{r_0^{5/3} L_0^{1/3}} \left[2F\left(\frac{1}{2}\Delta\boldsymbol{\rho}'\right) + 2F(\boldsymbol{d}) - F\left(\boldsymbol{d} + \frac{1}{2}\Delta\boldsymbol{\rho}'\right) - F\left(\boldsymbol{d} - \frac{1}{2}\Delta\boldsymbol{\rho}'\right) \right] \right\}.}$$

Or, alternatively,

$$\boxed{\begin{aligned}
\mu_{\text{turb,mvK}} = \exp\Bigg\{ -\frac{1}{2} \Bigg[& 2D_{\text{mvK}}\left(\frac{1}{2}\Delta\boldsymbol{\rho}'\right) + 2D_{\text{mvK}}(\boldsymbol{d}) - D_{\text{mvK}}\left(\boldsymbol{d} + \frac{1}{2}\Delta\boldsymbol{\rho}'\right) \\
& - D_{\text{mvK}}\left(\boldsymbol{d} - \frac{1}{2}\Delta\boldsymbol{\rho}'\right) \Bigg] \Bigg\}.
\end{aligned}}$$

B.3 Generalization

Both previous results can be written in terms of a generic phase structure function $D_{\mathcal{M},r_0}$, where $\mathcal{M}$ denotes the chosen turbulence model:

$$\boxed{\begin{aligned}
\mu_{\text{turb},\mathcal{M}}(r_0) = \exp\Bigg\{ -\frac{1}{2} \Bigg[& 2D_{\mathcal{M},r_0}\left(\frac{1}{2}\Delta\boldsymbol{\rho}'\right) + 2D_{\mathcal{M},r_0}(\boldsymbol{d}) - D_{\mathcal{M},r_0}\left(\boldsymbol{d} + \frac{1}{2}\Delta\boldsymbol{\rho}'\right) \\
& - D_{\mathcal{M},r_0}\left(\boldsymbol{d} - \frac{1}{2}\Delta\boldsymbol{\rho}'\right) \Bigg] \Bigg\}.
\end{aligned}}$$

Here $D_{\mathcal{M},r_0}$ is the phase structure function for either the Kolmogorov or modified von Kármán model. Its dependence on r_0 determines the theoretical dependence of the turbulence factor, and therefore of the concurrence, on the turbulence strength.

C Generated Phase Screens

Below are displayed some examples of static phase screens generated via the framework developed for this work.

(a) Kolmogorov (Seed $s = 137$)

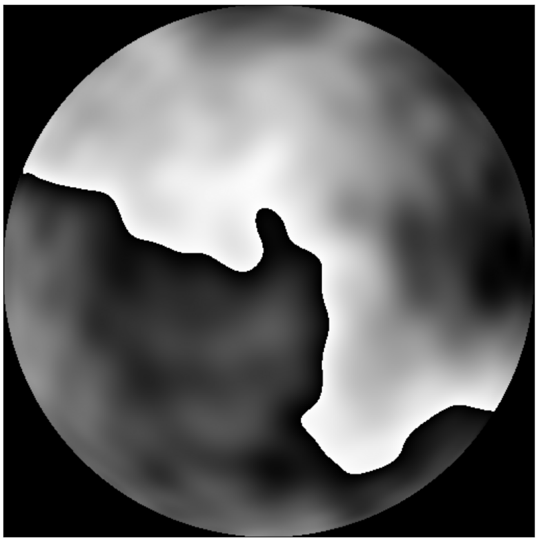

(b) von Kármán (Seed $s = 137$)

(c) Kolmogorov (Seed $s = 6767$)

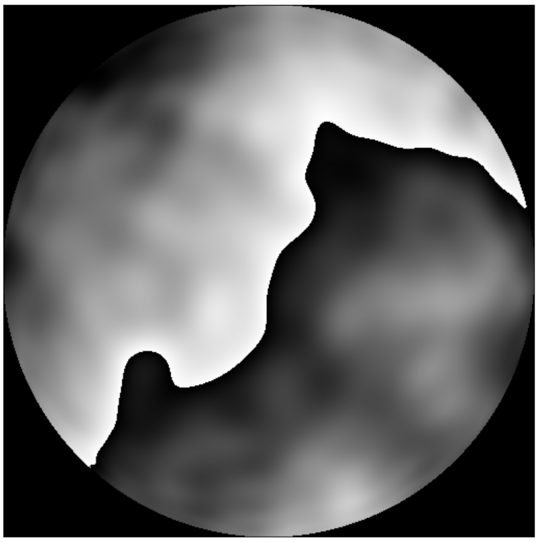

(d) von Kármán (Seed $s = 6767$)

Figure 6: Comparison of phase screens generated by the Kolmogorov (left column) and modified von Kármán (right column) turbulence models using identical random seeds. The top row uses seed $s = 137$, and the bottom row uses seed $s = 6767$. Parameters are held constant across all images at $D = 2$ cm, $r_0 = 0.5$ cm, $L_0 = 10$ m, and $l_0 = 1$ mm. Note the structural similarities dictated by the shared seeds, with high and low-frequency characteristic differences resulting from the choice of spectral model.

D Adaptive Sampling

In the numerical simulations, each value of concurrence requires the generation of an ensemble of random phase screens and the evaluation of the turbulence factor μ_{turb} at the four transverse positions that define the spatial two qubit state. Therefore, evaluating the concurrence for many uniformly distributed values of Fried's parameter r_0 is computantionally expensive. In order to reduce the number of evaluations while still resolving the general shape of the curve, an adaptive sampling algorithm was implemented.

The main goal of the method is to concentrate numerical evaluations od $\mathcal{C}(r_0)$ in the parts where the function changes the most. This is useful because depending on the geometrical parameters of the two photon system and on the selected turbulence model, concurrence may either vary slowly with r_0 or change rapidly in a narrow range.

Let the numerically estimated concurrence be written as

$$\widehat{\mathcal{C}}(r_0) = \left| \frac{1}{N_\mathrm{s}} \sum_{n=1}^{N_\mathrm{s}} \exp\left[-i\left(\phi_n(\boldsymbol{r}_{s1}) - \phi_n(\boldsymbol{r}_{s2}) + \phi_n(\boldsymbol{r}_{i1}) - \phi_n(\boldsymbol{r}_{i2})\right)\right] \right|, \tag{58}$$

where N_s is the number of generated phase screens and ϕ_n is the n-th random phase screen. The adaptive algorithm treats this evaluation as an expensive function call.

The first step of the method is to evaluate concurrence at the endpoints of a selected interval

$$r_{0,\mathrm{min}} \le r_0 \le r_{0,\mathrm{max}}. \tag{59}$$

For any already sampled interval $[a, b]$, the midpoint

$$m = \frac{a+b}{2} \tag{60}$$

is evaluated. The concurrence expected at the midpoint from a straight line connecting the two endpoints is

$$\widehat{\mathcal{C}}_\mathrm{lin}(m) = \frac{\widehat{\mathcal{C}}(a) + \widehat{\mathcal{C}}(b)}{2}. \tag{61}$$

The local deviation from this linear behavior is then estimated as

$$\varepsilon_{[a,b]} = \left| \widehat{\mathcal{C}}(m) - \widehat{\mathcal{C}}_\mathrm{lin}(m) \right|. \tag{62}$$

A larger value of $\varepsilon_{[a,b]}$ indicates that the concurrence curve is less linear inside that interval, which means that additional points are useful there. To avoid selecting only very small intervals with small absolute relevance, the priority score used in the implementation was

$$S_{[a,b]} = \varepsilon_{[a,b]}(b-a). \tag{63}$$

At each step, the interval with the largest score is selected and split into two subintervals, $[a, m]$ and $[m, b]$. The process is repeated until either a maximum number of sampled points is reached or the largest estimated error is below a predefined tolerance.

The algorithm can be summarized as follows:

1. Evaluate $\widehat{\mathcal{C}}(r_{0,\mathrm{min}})$ and $\widehat{\mathcal{C}}(r_{0,\mathrm{max}})$.
2. For each active interval $[a, b]$, evaluate its midpoint $m = (a + b)/2$.
3. Compute the local error estimate $\varepsilon_{[a,b]}$ from Eq. (62).
4. Assign the interval priority score $S_{[a,b]}$ from Eq. (63).
5. Select the interval with the largest score and divide it into two new intervals.
6. Repeat until the stopping criterion is reached.

E Individual Simulation Results

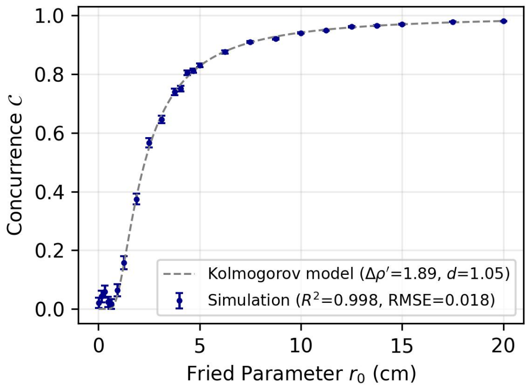

(a) Kolmogorov: $\rho_{s2} = (0.05, 0.0)$

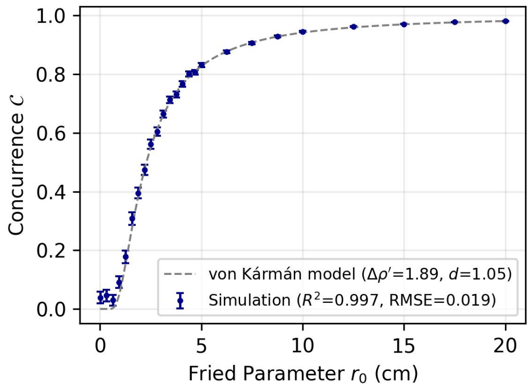

(b) von Kármán: $\rho_{s2} = (0.05, 0.0)$

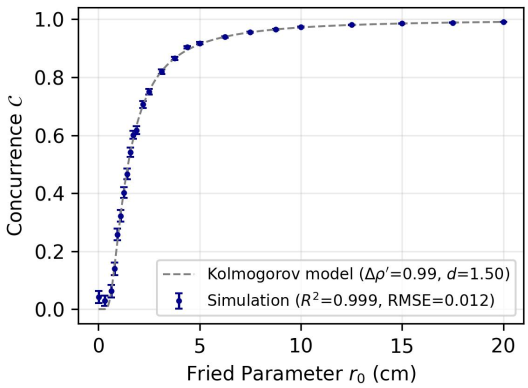

(c) Kolmogorov: $\rho_{s2} = (0.5, 0.0)$

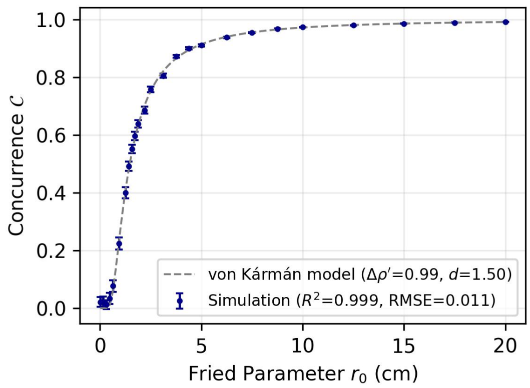

(d) von Kármán: $\rho_{s2} = (0.5, 0.0)$

Figure 7: Comparison of theoretical models and numerical simulations for the concurrence $\mathcal{C}$ as a function of the Fried parameter r_0. The left column represents data fitted to the Kolmogorov model, while the right column shows the modified von Kármán model. Each row details a specific spatial configuration, with ρ_{s1} fixed at $(1.0, 0.0)$ and varying ρ_{s2} coordinates. Error bars indicate the standard deviation of the simulated data. (Part 1 of 2)

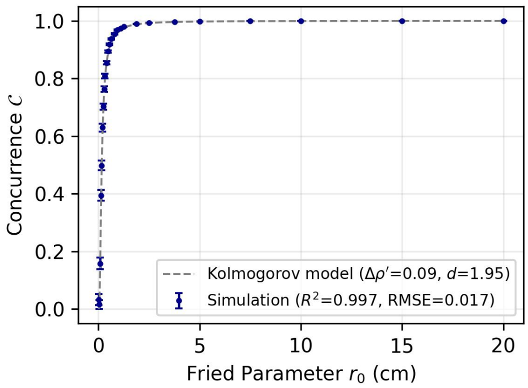

(e) Kolmogorov: $\rho_{s2} = (0.95, 0.0)$

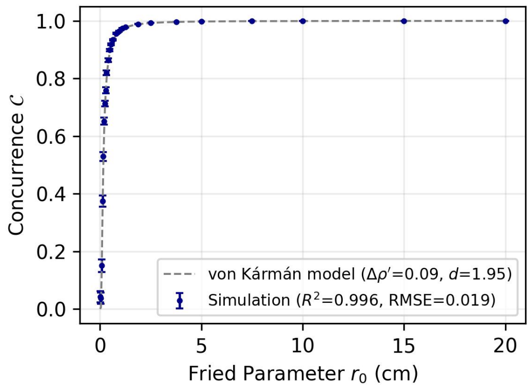

(f) von Kármán: $\rho_{s2} = (0.95, 0.0)$

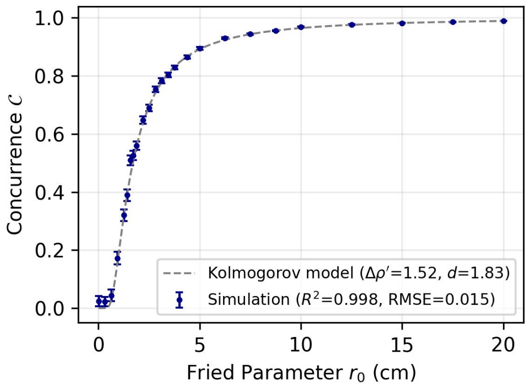

(g) Kolmogorov: $\rho_{s2} = (0.7, 0.7)$

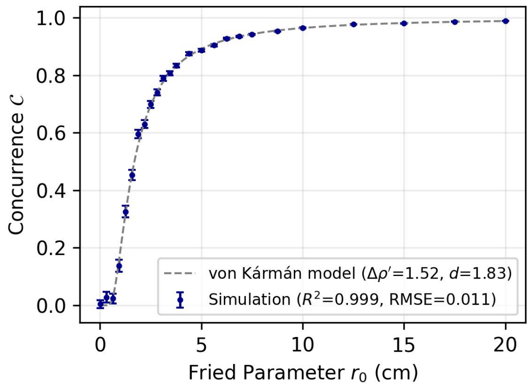

(h) von Kármán: $\rho_{s2} = (0.7, 0.7)$

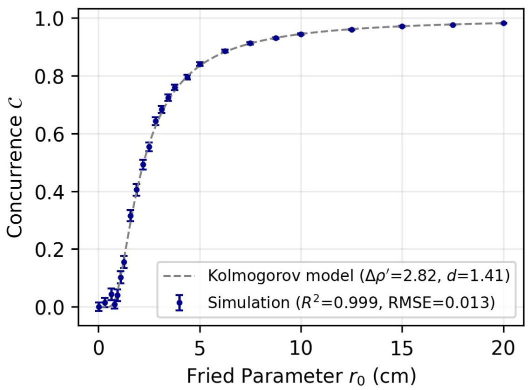

(i) Kolmogorov: $\rho_{s2} = (0.0, 1.0)$

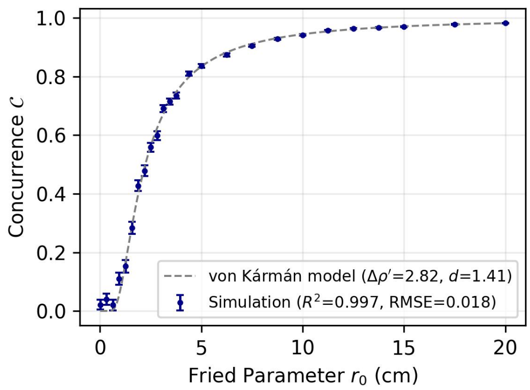

(j) von Kármán: $\rho_{s2} = (0.0, 1.0)$

Figure 7: Comparison of theoretical models and numerical simulations (Continued). The high R^2 values indicate excellent agreement between the simulation and theoretical approximations.